Acta Pharmaceutica Sinica B 2025;15(8):4137−4155

Chinese Pharmaceutical Association
Institute of Materia Medica, Chinese Academy of Medical Sciences

Acta Pharmaceutica Sinica B

www.elsevier.com/locate/apsb
www.sciencedirect.com

ORIGINAL ARTICLE

Chemical knockdown of Keap1 and homoPROTAC-ing allergic rhinitis

Jianyu Yan[a,†], Tianyu Wang[c,†], Ruizhi Yu[a,†], Lijuan Xu[a,†], Hongming Shao[a], Tengfei Li[c], Zhe Wang[c], Xudong Cha[c], Zhenyuan Miao[a], Chengguo Xing[d], Ke Xu[b,*], Huanhai Liu[c,*], Chunlin Zhuang[a,*]

[a]*The Center for Basic Research and Innovation of Medicine and Pharmacy (MOE), School of Pharmacy, Naval Medical University/Second Military Medical University, Shanghai 200433, China*
[b]*Shanghai Key Laboratory of Anesthesiology and Brain Functional Modulation, Clinical Research Center for Anesthesiology and Perioperative Medicine, Translational Research Institute of Brain and Brain-Like Intelligence, Shanghai Fourth People's Hospital, School of Medicine, Tongji University, Shanghai 200434, China*
[c]*Department of Otolaryngology, Changzheng Hospital, Naval Medical University/Second Military Medical University, Shanghai 200003, China*
[d]*Department of Medicinal Chemistry, University of Florida, Gainesville, FL 32610, USA*

Received 13 November 2024; received in revised form 12 March 2025; accepted 23 April 2025

KEY WORDS

Allergic rhinitis;
Keap1;
Nrf2;
E3 ligase;
Degradation;
HomoPROTAC

Abstract Allergic rhinitis (AR), a globally prevalent immune-mediated inflammatory condition, is still an incurable disease. In the present study, we have validated the impact of the Kelch-like ECH associated protein 1 (Keap1)-related oxidative stress and inflammatory response in clinical AR patient peripheral blood and nasal swab samples, emphasizing the biological relevance of Keap1 and AR. Targeting Keap1 -nuclear factor erythroid 2-related factor 2 (Nrf2) related anti-oxidative stress may be effective for AR intervention. Drawing inspiration from the Keap1 homodimerization and the E3 ligase characteristics, we herein present a design of novel bivalent molecules for chemical knockdown of Keap1. For the first time, we characterized ternary complexes of Keap1 dimer and one molecule of bivalent compounds. The best bivalent molecule **8** encompasses robust capacity to degrade Keap1 as a homoPROTAC^{KEAP1}. It efficaciously suppresses inflammatory cytokines in extensively different cells, including human nasal epithelial cells. Moreover, in an AR mouse model, we confirmed that the chemical degradation induced by homoPROTAC^{KEAP1} led to therapeutic benefits in managing AR symptoms, oxidative stress and

*Corresponding authors.
E-mail addresses: kx2129@tongji.edu.cn (Ke Xu), liuhuanhaiok@smmu.edu.cn (Huanhai Liu), zclnathan@163.com (Chunlin Zhuang).
[†]These authors made equal contributions to this work.
Peer review under the responsibility of Chinese Pharmaceutical Association and Institute of Materia Medica, Chinese Academy of Medical Sciences.

https://doi.org/10.1016/j.apsb.2025.05.025

inflammation. In summary, our findings underscore the efficacy of targeting the Keap1 system through the homoPROTAC-ing technology as an innovative and promising treatment strategy for the incurable allergic disorders.

1. Introduction

Allergic rhinitis (AR) affects approximately 15% of adults in the United States (∼50 million individuals) and about 18% of adults (∼250 million individuals) in China, as well as notable percentage of children[1-4]. However, it is still an incurable disease. It has been characterized to be caused by an immunoglobulin E (IgE)-mediated immune inflammation to inhaled allergens[5,6]. It encompasses a diverse range of clinical symptoms, with rhinorrhea and nasal congestion being the most prevalent[2,4,7]. In addition, more severe conditions such as asthma, chronic or recurrent sinusitis, headaches, as well as sleep problems affect quality of life, and even lead to depression[2,8,9]. With these problems, AR is causing underestimated and substantial economic burden and disability worldwide[10].

For clinical management, continuous allergen avoidance should be the first choice for AR patients[8]. Many pharmacotherapy options are available for AR to encompass symptomatic managements[2,8]. Antihistamines (oral and/or intranasal) and corticosteroids (intranasal), sometimes, coupled with anti-inflammatory medications are administrated depending on the severity, yet these interventions frequently fall short of achieving complete efficacy. Allergy immunotherapy (AIT), embodied through subcutaneous and sublingual approaches, holds significant potential for effectiveness[11]. However, concerns over safety, inconvenience, the lengthy treatment duration spanning several years, and poor adherence among patients hinder its widespread acceptance[12]. Hence, scientists globally have embarked on a relentless effort to discover novel therapeutic interventions. Asthma and AR frequently coexist, displaying a profound interconnection that prompts us to mirror the pathogenesis of asthma in searching effective interventions[6,13]. Exceeding reactive oxygen species (ROS), naturally occurring byproducts of cellular metabolism, can lead to oxidative stress, contributing to a wide range of diseases[14]. Early in 2002, Crapo and his colleagues highlighted the involvement of oxidative stress in mediating the activity of allergic respiratory diseases[15]. The intricate interplay between oxidative stress and asthma pathogenesis has been highlighted[16-20]. It is revealed that blood leukocytes sourced from asthmatic patients exhibited elevated levels of superoxide anion and diminished concentrations of glutathione (GSH). Blood markers of oxidative stress were also changed, including increased levels of protein carbonyls, nitrites/nitrates, uric acid and lipid peroxides, alongside reduced activity of glutathione peroxidase and lower GSH concentrations. In recent years, growing evidence has emerged, implicating oxidative stress as a pivotal factor in the pathogenesis of AR[21]. The oxidative stress markers, such as malondialdehyde (MDA), and nuclear factor erythroid 2-related factor 2 (Nrf2), were found to be dysregulated in the OVA-induced AR model[22,23]. *Piper nigrum* extract was found to inhibit allergic responses and protect from nasal epithelial barrier dysfunction *via* activation of Nrf2 transcription factors in the AR model[24]. In human, Koksal et al.[25] found the oxidative biomarkers including total oxidant status (TOS), total antioxidant status (TAS), and oxidative stress index (OSI) in nasal lavage fluid (NALF) were dysregulated, highlighting the association between AR and oxidative stress. Therefore, targeting oxidative stress signaling and related enzymes may be effective for AR intervention.

Nrf2, a key regulator in the oxidative stress pathway, is inhibited by Kelch-like ECH-associated protein 1 (Keap1) to maintain cell homeostasis[26,27]. Normally, Keap1 homodimerizes and binds to Nrf2 and facilitates the ubiquitination and subsequent proteasomal degradation[27]. With various stresses, Keap1-reactive cysteines are covalently modified, leading to the release of Nrf2 and blocking its degradation[28,29]. Modulating the Keap1−Nrf2 pathway through the utilization of either covalent electrophiles or noncovalent protein−protein interaction (PPI) inhibitors has effectively activated Nrf2 and possess remarkable efficacy in conferring a broad spectrum of diseases[30,31]. Notably, Keap1 functions as an adaptor protein within the Cullin-RING E3 ubiquitin ligase system, facilitating the ubiquitination of Nrf2[32]. However, the covalent electrophiles of Keap1 may lead to undesired cytotoxicity[26]. Significant efforts have been focused on developing monovalent PPI inhibitors that bind to Keap1 and subsequently activate Nrf2 in a delayed manner[14,33]. Nevertheless, this approach has not fully capitalized on the Keap1 homodimerization process, leaving one molecule of Keap1 available for potential alternative interactions. Recognizing this limitation, the Jiang group has recently designed bivalent Keap1 inhibitors that demonstrate enhanced potency by more effectively targeting the homodimerization interface[34]. However, these advances have yet to incorporate the E3 ligase characteristics of Keap1 for degrading. Consequently, we propose a novel hypothesis: designing a bifunctional compound, named homobivalent proteolysis-targeting chimeras of degrading Keap1 (homoPROTAC^{KEAP1}), based on our understanding of Keap1 homodimerization and its E3 ligase activity. This approach aims to achieve chemical knockdown of Keap1 by harnessing the ubiquitin−proteasome system, potentially representing a groundbreaking strategy for the treatment of AR.

Here, we employed a crystallography-driven approach to meticulously engineer homodimers incorporating different linkers and ultimately identified a potent homoPROTAC^{KEAP1} **8**. Biophysical assays and X-ray crystallographic generation of the ternary complexes definitively established the bivalent binding mechanism. In multiple cells, homoPROTAC^{KEAP1} **8** demonstrated robust capacity to degrade Keap1 and efficaciously suppressed inflammatory cytokines. Furthermore, we conducted thorough validation of oxidative stress, inflammatory responses, and the Keap1−Nrf2 pathway in the context of AR, leveraging clinical patient peripheral blood and nasal swab samples. In human nasal epithelial cells, the molecule exerted chemical degradation effect as biological knockdown of Keap1. Extending

our findings to an animal model, we further validated the homoPROTAC-ing effect on AR, positioning it as an innovative treatment strategy for the incurable allergic disorders.

2. Results

2.1. Crystallography-driven design identifies compound 8 as a homodimer inhibitor of Keap1−Nrf2 interaction

Our group previously reported a nanomolar inhibitor of Keap1−Nrf2 interaction, NXPZ-2, as well as the crystal complex of human Keap1 Kelch domain with the inhibitor (PDB code: 7XM2, Fig. 1A)[35,36]. We observed the solvent exposed area of Keap1 for optimization, resulting in more potent inhibitors, including 6k, POZL and their crystal complexes with Keap1 (PDB codes: 7XM3 and 7XOT)[31,35]. Here, in the crystallographic study, we have further identified a unique dimerization pattern of the Keap1 protein with a "face-to-face" configuration feature, confirming the existence of Keap1 dimer (PDB code: 9J70, Fig. 1B). Notably, the solvent exposed position is situated at the center of this arrangement, indicating a new pocket for designing bivalent molecules. The distance between the two individual molecules of Keap1 protein is relatively short, allowing for the accommodation of a monovalent inhibitor equipped with suitable spacers or linkers within each of them. This design strategy effectively mimics the Keap1 homodimerization process, enabling it to function as an E3 ligase, thereby facilitating the "self-degradation" of Keap1 and promoting the dissociation of Nrf2 from its binding with Keap1 dimer.

The novel bivalent compounds were synthesized through a single-sided linkage at the amino group present on the benzosulfamide moiety (Fig. 1C and Supporting Information Scheme S1). These compounds (**1**−**10**) incorporated two distinct types of spacers/linkers: alkyl chains (**1**−**4**) and polyethylene glycol (PEG) chains (**5**−**10**), both assembling with two amides. Our findings revealed that all analogues, with the exception of compounds **3** and **4**, demonstrated remarkable inhibitory activity against the Keap1−Nrf2 interaction, operating within the nanomolar range, as accurately assessed through a fluorescent anisotropy assay (Fig. 1D). Among them, compounds **1**, **5**, **6**, **8**, and **10** possessed K_{D2} values of <100 nmol/L. Compounds **7** and **9** showed moderate affinities of 136 and 111 nmol/L. In particular, compound **8** excelled with a best K_{D2} value of 41 nmol/L, outperforming the monovalent NXPZ-2, which had a K_{D2} of 53 nmol/L. Microscale thermophoresis (MST) was employed as a second biophysics method to cross-validate the biomolecular interactions between the compounds and the Keap1 protein[37]. Consistently, we detected the MST traces and fitted K_d values of 45 nmol/L for NXPZ-2 (Fig. 1E) and 29 nmol/L for compound **8** (Fig. 1F). Next, size exclusion chromatography (SEC) was used to validate the ability of the bivalent compound **8** to induce the formation of ternary complex[38]. We found that Keap1 protein migrates more quickly in the presence of compound **8**, relative to DMSO control (Fig. 1G and Supporting Information Fig. S1A−S1F). Upon calibration using globular proteins that serve as proxies for the Keap1 monomer, the presence of increasing amounts of active compounds augmented the formation of the Keap1 dimer, achieving its maximum intensity at a ratio of 2:1. Notably, the shifted peak at a volume of 14.3 mL (flow rate: 0.6 mL/min), corresponded to a molecular weight of approximately 64 kDa, indicating the peak corresponds to the ternary complex $(Keap1)_2$: (compound $\mathbf{8})_1$.

Crystallography is the gold standard for both elucidating structural insights, particularly in binary protein/ligand interactions[39]. Consequently, we determined a ternary crystal structure of Keap1 dimer in complex with a single molecule of compound **8** at a resolution of 3 Å for the first time (PDB code: 9J7G, Fig. 1H), confirming the result of SEC assay. The binding pocket of two Keap1 monomers also face to each other as the dimer crystal (Fig. 1B). Notably, in addition to the core structure comprising two NXPZ-2 moieties, a significant density of linker moieties that interconnect these two components within compound **8** is discernible (Fig. 1K). The binding pockets of Keap1−compound **8** are very similar with other complexes, and the NXPZ-2 moiety of compound **8** form an extensive interaction network with Keap1, which is the same as interactions between Keap1 and NXPZ-2 (Fig. 1I and J). The hydrogen-bonding interactions between residues of Keap1 and the linker moiety of compound **8** are clearly illustrated, improving the interactions between Keap1 and **8**. Specifically, Arg336 and Tyr572, both residing on a Keap1 monomer, engage in the formation of two distinct hydrogen bonds with two oxygen atoms present on the linker moiety of **8** (Fig. 1J). Meanwhile, the density of most of the linker moiety can be observed plausibly due to these interactions (Fig. 1H and K). Besides, we also obtained the ternary crystal complexes of Keap1 dimer with **1** (PDB code: 9J7F, Fig. S1G−S1J) and 7 (PDB code: 9J71, Fig. S1K−S1N). The density of linker moiety of compound 1 with the shortest linker is visible, and no interaction between linker moiety and Keap1 is detected due to an alkyl chain within the compound. In the Keap1−compound **7** ternary complex, Gln530 of one protein establishes a hydrogen bond with the carbonyl group situated within the linker region. Data collection and refinement statistics for the complexes are presented in Supporting Information Table S1. The visible linker moiety densities of the ternary complex suggest that introduction of polar atom such as nitrogen and oxygen into the linker part, as well as the linker length can facilitate the stabilization and visualization of linker density and enhance the interaction between Keap1 and the bivalent compounds. The fluorescent anisotropy-derived K_{D2} values strengthen the hypothesis, demonstrating better binding affinity of bivalents with PEG chains than those with alkyl chains.

2.2. Compound 8 possesses the best self-degradation efficiency as a homoPROTAC of Keap1 in MDA-MB-231 cells

We first selected the MDA-MB-231 cell line, which exhibits a satisfactory level of Keap1 protein expression, for evaluating the degradation efficiency of bivalent compounds[40]. Eight bivalents, excluding compounds **3** and **4** with low Keap1−Nrf2 PPI inhibitory activities, were assessed for their effects on Keap1 protein levels through Western blotting analysis. No apparent cytotoxicity of these compounds was demonstrated at 100 μmol/L (Supporting Information Fig. S2A). We separately treated MDA-MB-231 cells with 0.1−3 μmol/L of compounds and monitored the change of Keap1 at a time point of 24 h (Fig. 2A−C, Fig. S2B and S2C). At the concentration of 3 μmol/L, protein levels were significantly reduced when treated with compounds 5 (D_{max} = 95%, Fig. 2B), **7** (D_{max} = 64%), **9** (D_{max} = 59%), and **10** (D_{max} = 67%). At the concentration of 0.1 μmol/L, compound **5** still showed a reduction of about 50%, and particularly, compound **8** exerted the

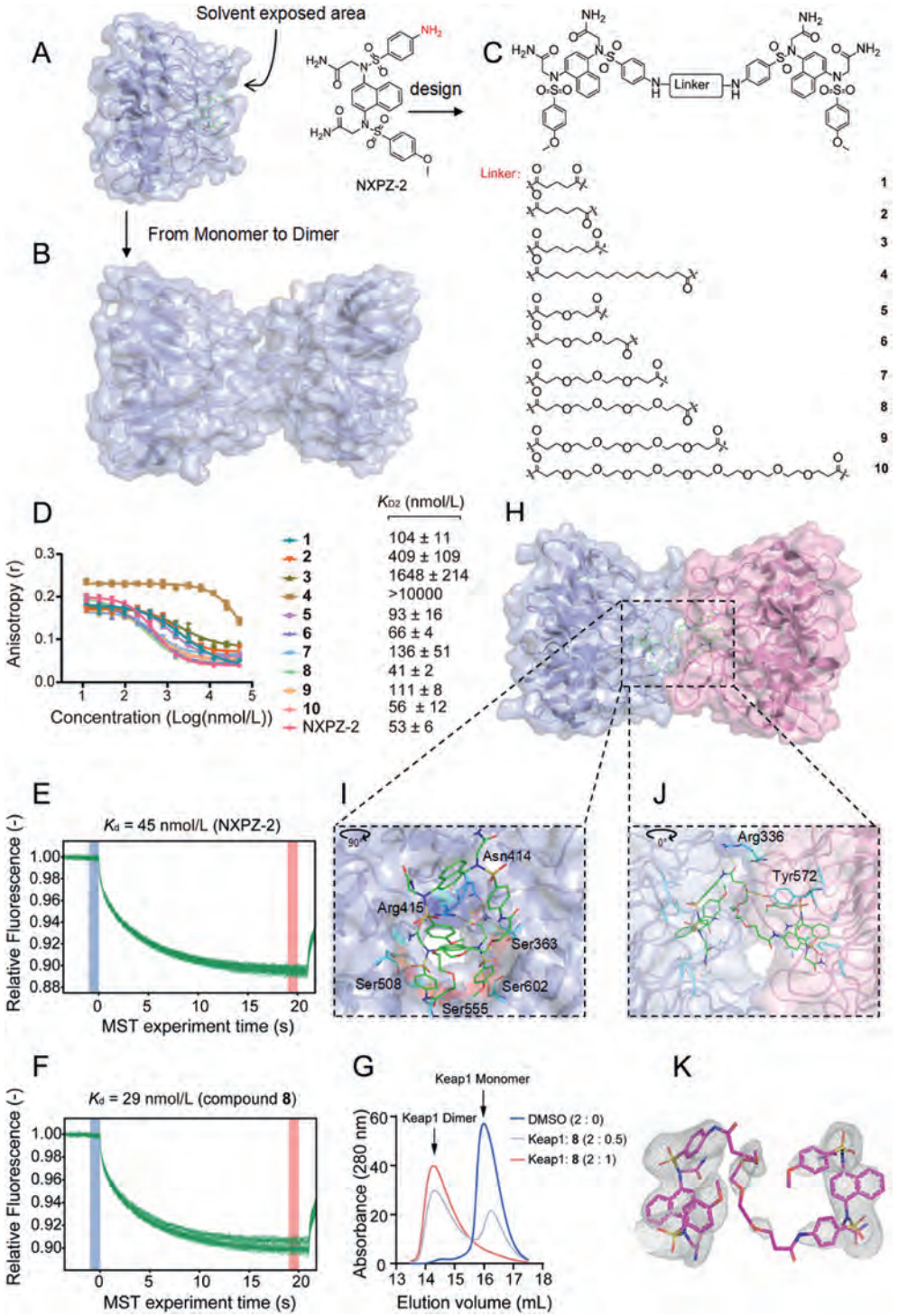

Figure 1 Crystallography-driven design identifies compound **8** as a homodimer inhibitor of Keap1−Nrf2 interaction. (A) The crystal complex of Keap1 and NXPZ-2 (PDB code: 7XM2) in the surface and cartoon types and the chemical structure of NXPZ-2. (B) The crystal complex of dimerized Keap1 (PDB code: 9J70) in the surface and cartoon types. (C) The design of bivalent compounds **1**−**10** and their chemical structures. (D) The dose−response curves for the binding affinity (K_{D2}) of the ten compounds and NXPZ-2 with Keap1 protein generated by a fluorescence anisotropy assay. Data representative of $n = 3$ independent experiments as mean ± SD. (E) The MST-trace chart of NXPZ-2 with Keap1 for determining the binding affinity (K_d). Data representative of $n = 3$ independent experiments as average. (F) The MST-trace chart of compound 8 with Keap1 for determining the binding affinity (K_d). Data representative of $n = 3$ independent experiments as average. (G) UV chromatograms from SEC analysis. Keap1 and compound **8** alone or mixed at a ratio of 2:0.5 or 2:1 mol/L ratio, in the presence of excess DTT (1 mmol/L) avoiding the self-aggregation of Keap1 protein, were run on a Superdex 200 Increase 10/300 GL column. (H) The ternary crystal complex of one molecule of compound **8** combined with two molecules of Keap1 (PDB code: 9J7G). Two Keap1 proteins are shown in lightblue and pink cartoon (50% transparency) and surface (60% transparency) types respectively. Compound **8** is shown in green stick model. (I, J) Interactions between

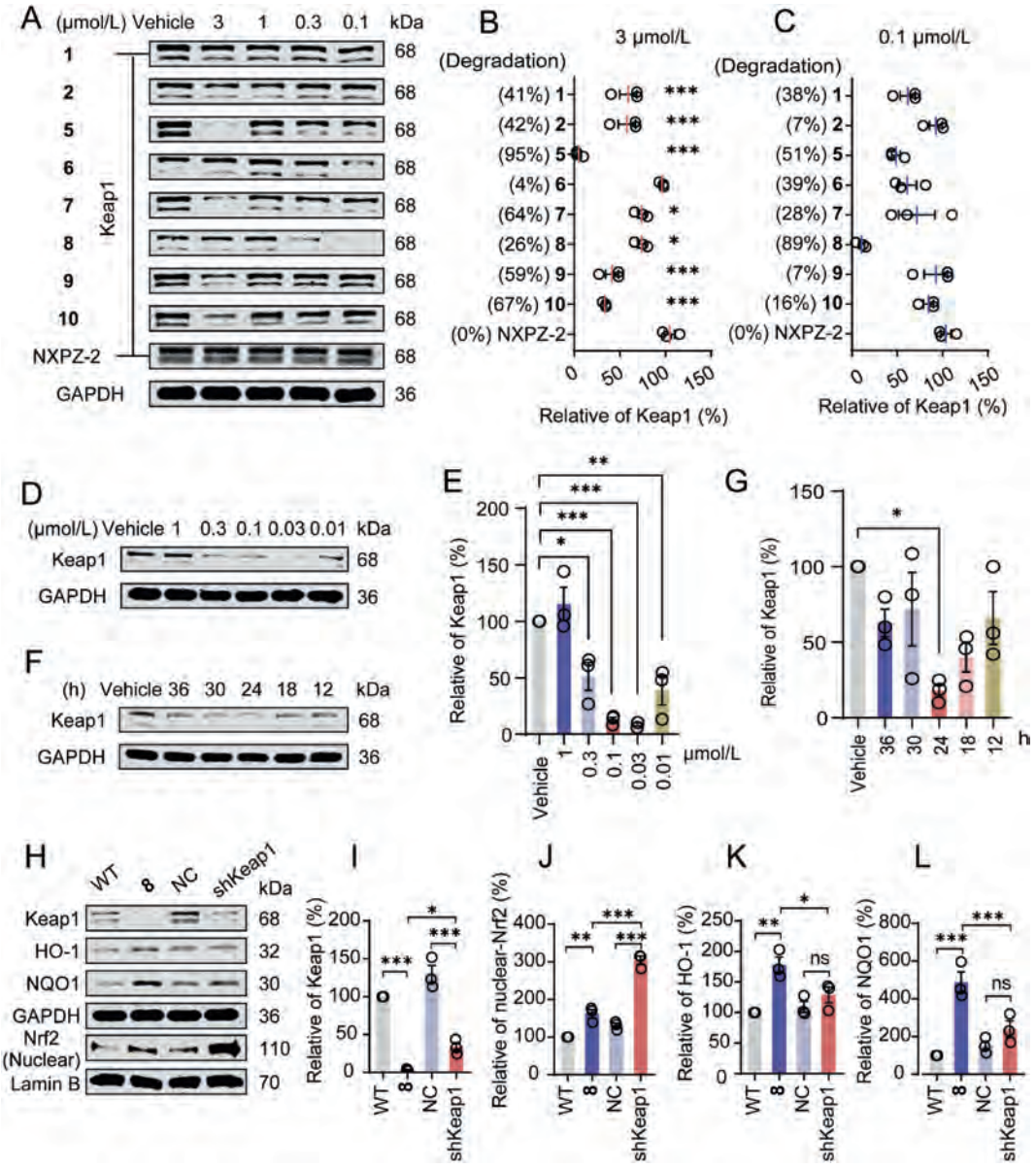

Figure 2 Compound **8** possesses the best self-degradation efficiency as a homoPROTAC of Keap1 in MDA-MB-231 cells. (A) The degradation efficiency screening of bivalent compounds treated with different concentrations (24 h) compared to the inhibitor NXPZ-2. (B) The gray-scale analysis of the degradation efficiency at 3 μmol/L ($n = 3$). (C) The gray-scale analysis of the degradation efficiency at 0.1 μmol/L ($n = 3$). (D, E) The dose-dependent effect on the degradation efficiency of compound **8** at 24 h, and the gray-scale analysis ($n = 3$). (F−G) The time-dependent effect on the degradation efficiency of compound **8** at 0.1 μmol/L, and the gray-scale analysis ($n = 3$). (H−L) Effects of chemical knockdown using compound **8** (0.1 μmol/L, 24 h) and biological knockdown using Keap1 knockdown lentivirus (shKeap1), as well as the subsequent changes in downstream gene expression (nuclear Nrf2, HO-1 and NQO1), and the gray-scale analysis ($n = 3$). Results are expressed as the mean ± SEM. $^*P < 0.05$; $^{**}P < 0.01$; $^{***}P < 0.001$.

degradation with a D_{max} of 89% (Fig. 2C). For comparison, the original NXPZ-2 was unable to elicit such a reduction under the same range of concentrations. Then, the protein synthesis was inhibited with cycloheximide (CHX) in HEK293T cells for re-screening the compounds. Compound **8** demonstrated remarkable persistence in its degradation capacity at a concentration of 0.1 μmol/L (D_{max} = 81%, Fig. S2D−S2F). However, unapparent degradation of Keap1 was observed upon treatment with other compounds, even in the higher concentrations (Fig. S2D−S2O).

Subsequently, we selected the best compound **8** and assessed the influence of varying concentrations (Fig. 2D and E, Fig. S2P and S2Q) in MDA-MB-231 cells. Our findings revealed that the

compound **8** and two Keap1 monomers. The compound and residues of Keap1 involved in compounds binding are labeled in cyan stick model. Hydrogen bonds are depicted as yellow dashed lines. (K) Omit Fo-Fc electron density at 3 Å resolution for compound **8** shown in magenta stick model, contoured at 2σ. Fig. 1A, B, H, J was generated using PyMol (http://pymol.sourceforge.net/).

concentrations of 0.03 and 0.1 μmol/L ($D_{max} > 90\%$) at 24 h showed the best efficacy. However, a notable observation was that protein levels significantly rebounded when the concentrations increased. This phenomenon aligns with the 'hook-effect' observed in high micromolar concentrations of bivalent compounds for von Hippel-Lindau (VHL)[38], which preferentially function as inhibitors of Keap1 rather than promoting its degradation. Here, the formation of binary 1:1 complex competes vigorously with, and ultimately prevails over, the establishment of the productive catalytic 2:1 complex, consistent with the SEC assay (Fig. 1G). We next evaluated the time-dependent degradation of compound **8** (Fig. 2F and G, Fig. S2R and S2S). Progressive removal of Keap1 protein over about 24 h was observed, degrading Keap1 level by about 50% already after 18 h of treatment (Fig. 2G). Interestingly, Keap1 levels increased again after 24 h, potentially due to the protein synthesis with a longer time as VHL[38]. The results together confirmed compound **8** could achieve almost complete degradation Keap1 protein level in MDA-MB-231 in 24 h.

As a bivalent compound for degradation, like a strategy for chemical knockdown, we further compared the efficiency of **8** with the biological knockdown of Keap1. We generated an Keap1-KD MDA-MB-231 cell line through lentivirus infection (shKeap1). We found the degradation of Keap1 was very similar to the efficiency of shKeap1 knockdown (Fig. 2H and I, Fig. S2T−S2V). As a regulator of Keap1, the Nrf2 is released from Keap1, and translocates to the nuclear for downstream transcription[30]. We found the nuclear Nrf2 was increased after treatment with **8**, as well as the shKeap1 group (Fig. 2J). Then, the downstream HO-1 and NQO1, were relatively elevated (Fig. 2K and L). The above findings indicate the bivalent **8** possesses the best self-degradation efficiency as a homoPROTAC of Keap1 in MDA-MB-231 cells.

2.3. The homoPROTAC exerts an extensive self-destruction of Keap1 mediated by the ubiquitin proteasomal system in a panel of cell lines, including human nasal mucosa epithelial cells

Initially, we endeavored to employ MG132, a potent inhibitor of proteasomal degradation, as a tool compound to decipher the underlying mechanism of compound **8**. However, our observations revealed an unexpected effect. MG132 itself was capable of decreasing Keap1 levels in MDA-MB-231 cells (Supporting Information Fig. S3A), echoing previous findings reported in HEK293T cells[41]. Therefore, these two cell lines might be unsuitable for further studies on mechanism.

We further validated the degradation scope and mechanistic insights of the homoPROTAC using a panel of different cell lines, including a human lung epithelial cell line, Beas-2B; a mouse macrophage cell line RAW264.7, a mouse Lewis lung carcinoma line LLC; and a mouse hepatocyte cell line AML-12. The cells were treated with compound **8**, and the result showed non-cytotoxic to the cells at 30 μmol/L (Fig. S3B). In Beas-2B cells, compound **8** demonstrated a robust ability to degrade Keap1 protein in a dose- and time-dependent manner. Optimal degradation of Keap1 was achieved at a concentration of 10 μmol/L, resulting in a significant reduction of 89% (24 h, Fig. 3A and C, Fig. S3G), and a similar high percentage of degradation at a time point of 48 h (10 μmol/L, 90%, Fig. 3B and D, Fig. S3H). The DC_{50} values were determined as 3.17 μmol/L in Beas-2B cells, 1.64 μmol/L in HNEpC cells, 1.11 μmol/L in LLC cells, and 2.98 μmol/L in RAW264.7 cells (Fig. S3C−S3F). Next, we ascertain whether the degradation process proceeds through the proteasomal degradation pathway. First, it was evidenced by the inability of compound 8 to degrade Keap1 in the presence of MG132 (0.1 μmol/L, Fig. 3M and N, Fig. S3M). Second, pretreatment with MLN4924 (0.3 μmol/L), which specifically inhibits the NEDD8-activating enzyme crucial for the neddylation and subsequent activation of cullin-RING E3 ubiquitin ligases, effectively blocked the degradation of Keap1. This finding corroborates the involvement of the proteasomal pathway in the degradation process. Similar findings were reproduced in RAW264.7 cells, where compound treatment resulted in nearly complete degradation of Keap1 protein at concentrations of 10 and 30 μmol/L (Fig. 3E and G, Fig. S3I). Additionally, a time-course analysis spanning 24−48 h further substantiated the effects (Fig. 3F and H, Fig. S3J). The dependency of this degradation on the proteasomal pathway was conclusively demonstrated (Fig. 3O and P, Fig. S3N). In LLC cells, we reconfirmed the degradation phenomenon, which was found to be comparable to the biological knockdown of Keap1 protein using LLC-KO cells (Fig. 3I−L, Fig. 3Q and R, Fig. S3K, S3L, S3O). Moreover, this degradation was also mediated through the proteasomal pathway, as well as in AML-12 cells (Fig. 3S and T, Fig. S3P). These findings indicate the homoPROTAC exerts an extensive self-destruction scope of Keap1 dependent on the cellular proteasomal machinery in a panel of cell lines.

Subsequently, we assessed the ability of homoPROTAC to degrade Keap1 in human nasal mucosa epithelial cells (HNEpC). In the cells, the homoPROTAC demonstrated a potent capability to degrade Keap1 protein in a dose- and time-dependent manner. The degradation was apparent at 3 μmol/L with a D_{max} of 71%, and achieved highest at 10 μmol/L with a D_{max} of 99% (Fig. 4A and B, Supporting Information Fig. S4A). The degradation showed a D_{max} of 78% at 12 h, and high percentages (>90%) at 24 and 48 h at a concentration of 10 μmol/L (Fig. 4C and D, Fig. S4B). The degradation could be also reduced by MG132 and MLN4924, confirming the involvement of the proteasomal pathway (Fig. 4E and F, Fig. S4C). In order to facilitate the detection of Keap1-bound ubiquitin, we selected a time point of 12 h for co-immunoprecipitation (Co-IP). The results showed that the ubiquitization of Keap1 in cells significantly increased with the treatment of **8** (Fig. 4G). In the immunofluorescence, Keap1 and ubiquitin were co-localized, showing strong green and red fluorescence in the Vehicle group. After 12 h of treatment with compound **8**, Keap1 (green fluorescence) significantly decreased, and highly coexpression of Keap1 and ubiquitin in cells were observed (Fig. 4H). We next generated an Keap1-KD HNEpC cell line through lentivirus infection (shKeap1). The degradation, leading to Nrf2 nuclear translocation, was also confirmed by shKeap1 (Fig. 4I−K, Fig. S4D). The downstream HO-1 and NQO1 were apparently increased with the homoPROTAC treatment (Fig. 4L and M). Besides, the results of electrophoretic mobility shift assay (EMSA) showed that the binding of Nrf2 to the downstream antioxidant response element (ARE) was also increased after the compound treatment (Fig. 4N). In Keap1-KD cells, the binding of Nrf2 to ARE in the nucleus was similarly increased. These results supported that the homoPROTAC treatment increased Nrf2 nuclear translocation and activated Keap1−Nrf2 pathway to reduce the oxidative stress.

Then, we assessed the anti-inflammatory efficacy of the homPROTAC, with comparison to NXPZ-2. Employing an inflammatory model induced initially with bacterial lipopolysaccharides (LPS), followed by a secondary stimulus in the form of

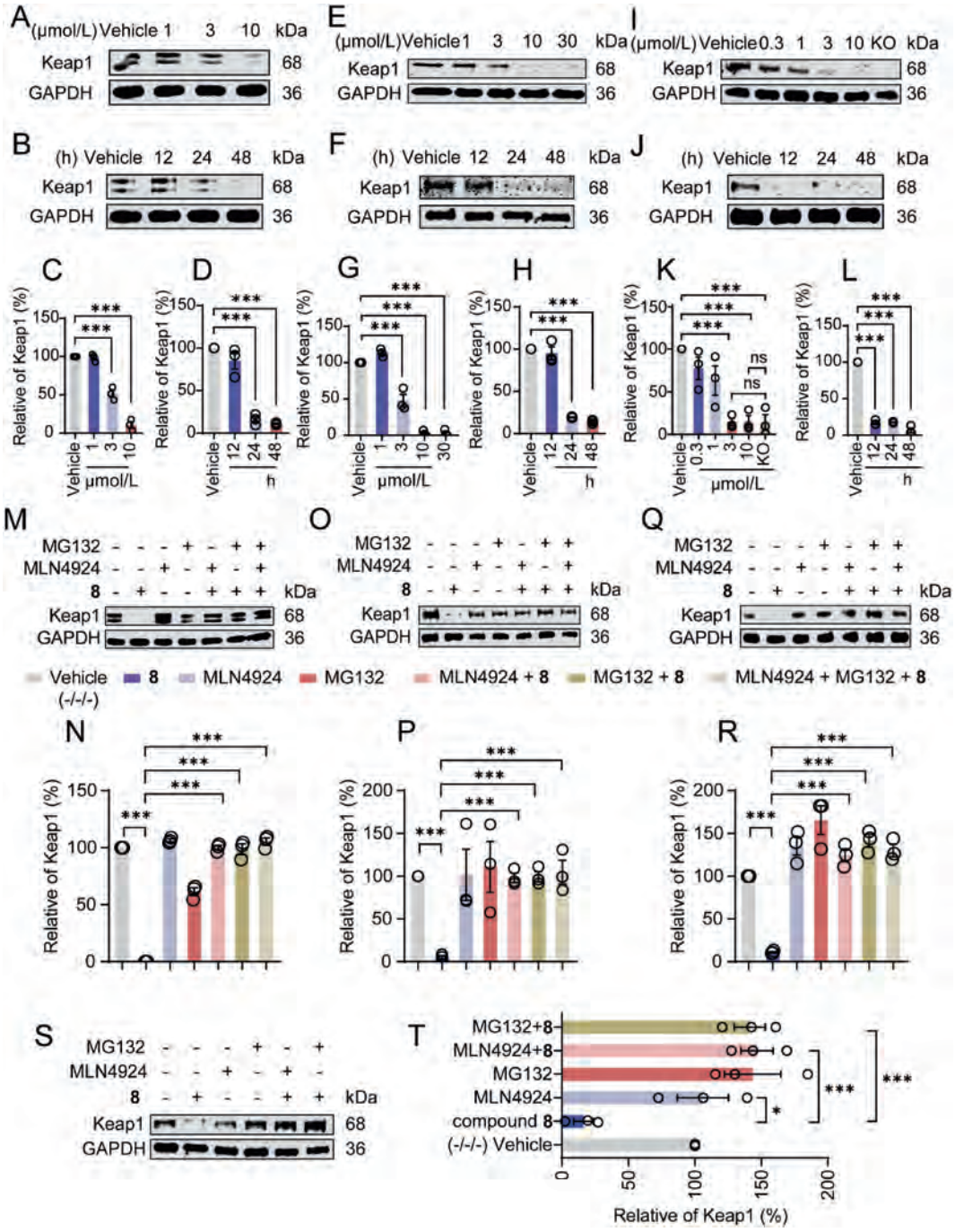

Figure 3 The homoPROTAC exerts an extensive self-destruction of Keap1 mediated by the ubiquitin proteasome system in a panel of cell lines. (A) The dose-dependent effect on the degradation efficiency of compound **8** at 24 h in Beas-2B cells. (B) The time-dependent effect on the degradation efficiency of compound **8** at 10 μmol/L in Beas-2B cells. (C, D) The gray-scale analysis of the degradation efficiency was determined in (A, B) ($n = 3$). (E) The dose-dependent effect on the degradation efficiency of compound **8** at 24 h in RAW264.7 cells. (F) The time-dependent effect on the degradation efficiency of compound **8** at 10 μmol/L in RAW264.7 cells. (G, H) The gray-scale analysis of the degradation efficiency was determined in (E, F) ($n = 3$). (I) The dose-dependent effect on the degradation efficiency of compound **8** at 24 h in LLC cells, and the comparison with Keap1 expression in Keap1-KO LLC cells. (J) The time-dependent effect on the degradation efficiency of compound **8** at 10 μmol/L in LLC cells. (K, L) The gray-scale analysis of the degradation efficiency was determined in (I, J) ($n = 3$). (M, N) The mechanism verification of the homoPROTAC for Keap1 degradation with or without MG132 (0.1 μmol/L) and MLN4924 (0.3 μmol/L) in Beas-2B cells at 24 h, and the gray-scale analysis ($n = 3$). (O, P) The mechanism verification of the homoPROTAC for Keap1 degradation with or without MG132 (0.1 μmol/L) and MLN4924 (0.3 μmol/L) in RAW264.7 cells at 24 h, and the gray-scale analysis. $n = 3$ biologically independent samples. (Q, R) The mechanism verification of the homoPROTAC for Keap1 degradation with or without MG132 (0.1 μmol/L) and MLN4924 (0.3 μmol/L) in LLC cells at 24 h, and the gray-scale analysis. $n = 3$. (S, T) The mechanism verification of the homoPROTAC for Keap1 degradation with or without MG132 (0.1 μmol/L) and MLN4924 (0.3 μmol/L) in AML-12 cells at 24 h, and the gray-scale analysis ($n = 3$). Results are expressed as the mean ± SEM. $^{*}P < 0.05$; $^{**}P < 0.01$; $^{***}P < 0.001$.

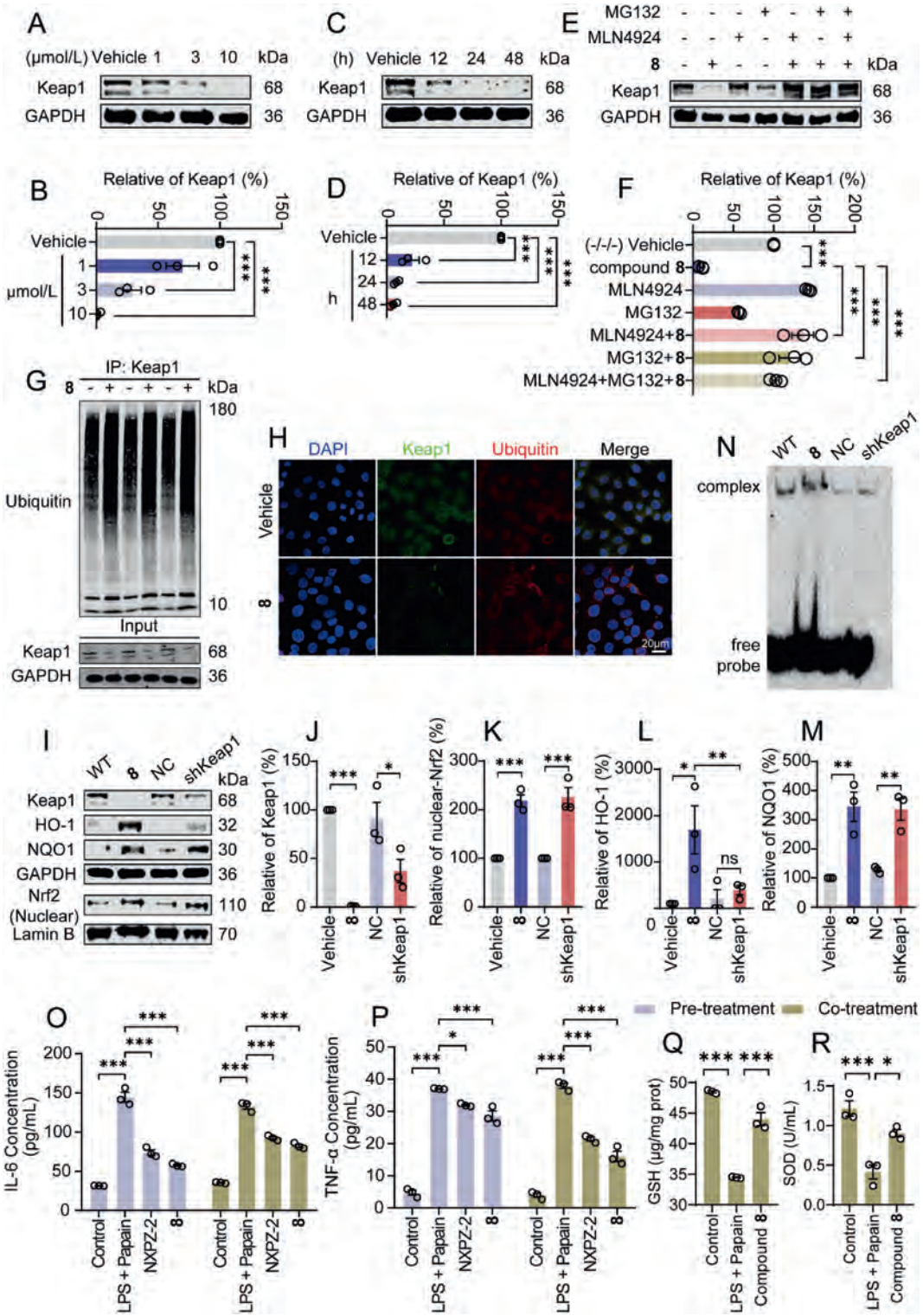

Figure 4 The homoPROTAC^{KEAP1} effectively degrades Keap1 protein and inhibits inflammation in human nasal mucosa epithelial cells. (A, B) The dose-dependent effect on the degradation efficiency of the homoPROTAC at 24 h in HNEpC cells, and the gray-scale analysis (n = 3). (C, D) The time-dependent effect on the degradation efficiency of the homoPROTAC at 10 μmol/L in HNEpC cells, and the gray-scale analysis (n = 3). (E, F) The mechanism verification of the homoPROTAC for Keap1 degradation with or without MG132 (0.1 μmol/L) and MLN4924 (0.3 μmol/L) in HNEpC cells at 24 h, and the gray-scale analysis (n = 3). (G) The ubiquitization level of Keap1 treated with or without compound **8** (10 μmol/L) was detected by Co-IP at 12 h (n = 3). (H) HNEpC cells were incubated with 10 μmol/L of **8** for 12 h, and subjected to Keap1 (green) and ubiquitin (red) immunofluorescence staining. DAPI was used to stain nuclei (blue). Merge: DAPI (blue), Keap1 (green), and ubiquitin (red). (Scale bar = 20 μm). (I–M) Effects of chemical knockdown using compound **8** (10 μmol/L, 24 h) and biological knockdown shKeap1, as well as the subsequent changes in downstream gene expression (nuclear Nrf2, HO-1 and NQO1), and the gray-scale analysis (n = 3). (N) The

allergen-derived protease papain[42], we tried two treatment strategies (pre- and co-treatments) to evaluate the effect (Fig. S4E). As a result, we observed a notable reduction in the levels of pro-inflammatory cytokines IL-6 (Fig. 4O) and TNF-α (Fig. 4P) upon two treatments with the homoPROTAC. Furthermore, this inhibitory effect surpassed that exhibited by NXPZ-2. In addition, the antioxidant capacity of HNEpC cells was restored after compound **8** treatment (Fig. 4Q and R). The anti-inflammatory effect (IL-6, TNF-α, NO levels) was confirmed using RAW264.7 cells (Fig. S4F−S4H). These findings underscore the significant potential of homoPROTAC as a potent tool for degrading Keap1 protein and its remarkable capacity to effectively reduce inflammation in HNEpC cells.

2.4. KEAP1-related oxidative stress and inflammation are dysregulated in the peripheral blood and nasal swabs of AR patients

To further identify the potential impact of Keap1-related oxidative stress on occurrence and development of AR, we collected a total of 15 human peripheral blood monoculear cell (PBMC) and nasal swab samples, including 10 AR patients and 5 control participants, for sequencing. Baseline demographic and clinic information is shown in Supporting Information Fig. S5A. There were no statistically significant differences in age and the male-to-female ratio between AR and control groups. The five AR patients had a long history of AR (13.10 $\pm$ 4.66 years), and 40% of them accompanied with a history of asthma. All the enrolled AR patients were in the symptom onset stage. Their total nasal symptom score (TNSS: 10.70 $\pm$ 1.19) and serum total IgE levels (IgE: 236.10 $\pm$ 128.24 pg/mL) were significantly higher than those in the control group (TNSS: 1.40 $\pm$ 1.02; IgE: 43.58 $\pm$ 19.30 pg/mL). Based on the criteria mentioned in the method part, high-quality mRNA samples were selected, comprising 10 PBMC samples (5 control participants and 5 AR patients), 15 nasal swab samples (5 control participants and 10 AR patients).

Through mRNA sequencing (mRNA-seq), we observed that the AR group exhibited 1122 significantly upregulated genes and 1155 significantly downregulated genes ($P < 0.05$, $|\log_2 FC| > 0.5$), compared to the control group (Fig. 5A). Notably, we found that *KEAP1*, an oxidative stress marker, as well as *IL4*, a classic inflammatory marker in AR, were significantly upregulated in the AR patients. The expression profiles of all differential genes identified through mRNA-seq, following enrichment analysis, are presented in the clustering heatmap in Fig. S5B. To investigate the potential role of *KEAP1* in development of AR, we conducted Gene Ontology (GO) and Kyoto Encyclopedia of Genes and Genomes (KEGG) enrichment analysis on all differentially expressed genes (DEGs, Fig. 5B and Fig. S5C). Particularly, the GO term enrichment analysis indicated that the DEGs were primarily associated with biological functions related to immune response, apoptosis, T cell activation, macrophage differentiation, and oxidative stress. To corroborate the findings from KEGG and GO term, the concentrations of oxidative stress indicators, glutathione (GSH) and superoxide dismutase (SOD), were measured. The results showed the antioxidant capacity of AR patients was significantly decreased (Fig. 5C and D). Next, focusing on the biological functions of *KEAP1*, we further identified the intersection between the oxidative stress related gene set and the DEG set, obtaining 56 downregulated genes and 58 upregulated genes (Fig. 5E). Through enrichment analysis, we determined that *KEAP1* was primarily involved in the oxidative stress response, cellular chemical stress response, and the processes of DNA-binding transcription factor binding (Fig. 5F). Integrated gene network was constructed by STRING database (minimum require interaction score >0.4) using oxidative stress related DEGs (Fig. 5G). *IL4* was undoubtedly one of the hub genes associated with oxidative stress related DEGs within the integrated gene network, in which its expression demonstrated a high interaction score with *ARG1* and *HMOX1*. Following the inclusion of downstream genes of *KEAP1*, including *HMOX1*, *NQO1* and *NFE2L2*, the network showed *KEAP1* was indeed identified as one of hub genes of oxidative stress related genes in AR. In addition, the heatmap was utilized to illustrate the specific expression of oxidative stress and inflammation related DEGs within the network, showing upregulated genes, including *IL4*, *KEAP1*, *CCR2*, *CCR5*, *CX3CR1*, and *TNFAIP8L2*, as well as downregulated genes such as *FOXO3*, *AREG*, *CREBBP*, and *BAG5* (Fig. 5H). To corroborate the findings from mRNA-seq of PBMCs, we conducted metatranscriptome on nasal swabs collected from AR patients and control participants. The overall DEGs profile was illustrated in Fig. S5D. We further employed the statistical analysis of metagenomic profiles (STAMP) software and identified the top 20 DEGs, exhibiting the most significant differences (Fig. S5E). The results showed that the expression of *KEAP1*, as one of the top 20 DEGs, was identified to be significantly upregulated in the AR group compared to the control group. Collectively, the above results indicated that *KEAP1*-related oxidative stress and inflammation might play an essential role in the occurrence or development of AR.

2.5. The homoPROTAC mitigates allergic nasal inflammation by regulating Keap1−Nrf2 pathway in the OVA-induced AR mouse model

Considering the relationship of the Keap1 pathway and AR occurrence, we tried to determine the therapeutic effect of the homoPROTAC *in vivo*. We constructed an AR mouse model through intraperitoneal (i.p.) sensitization with OVA for 3 weeks (i.p., once a week), followed by an intranasal (i.n.) challenge or treatment for 7 days (i.n., every day) (Fig. 6A). The allergic nasal symptoms, including number of nasal rubbing (Fig. 6B) and sneezing (Fig. 6C) every 10 min, were measured after the last OVA challenge. The behavioral tests showed the overall allergic symptoms of mice in the OVA group were significantly increased, compared to those of mice in the control group. The vehicle group as a negative control showed no difference in nasal symptoms compared to the control group. Dexamethasone (DEX), a glucocorticoid receptor agonist, was selected as a pharmacodynamic positive control[43]. We observed the allergic symptoms of mice

bindings of nuclear-Nrf2 to ARE of compound **8** (10 μmol/L, 24 h) after chemical and biological knockout of shKeap1 were detected by EMSA. (O, P) The changes in inflammatory factors IL-6 and TNF-α in the supernatant were detected by ELISA ($n = 3$). (Q) The change in oxidative marker GSH in the cells was detected by ELISA ($n = 3$). (R) The changes in oxidative marker SOD was detected in the supernatant by ELISA ($n = 3$). Results are expressed as the mean $\pm$ SEM. $^*P < 0.05$; $^{**}P < 0.01$; $^{***}P < 0.001$.

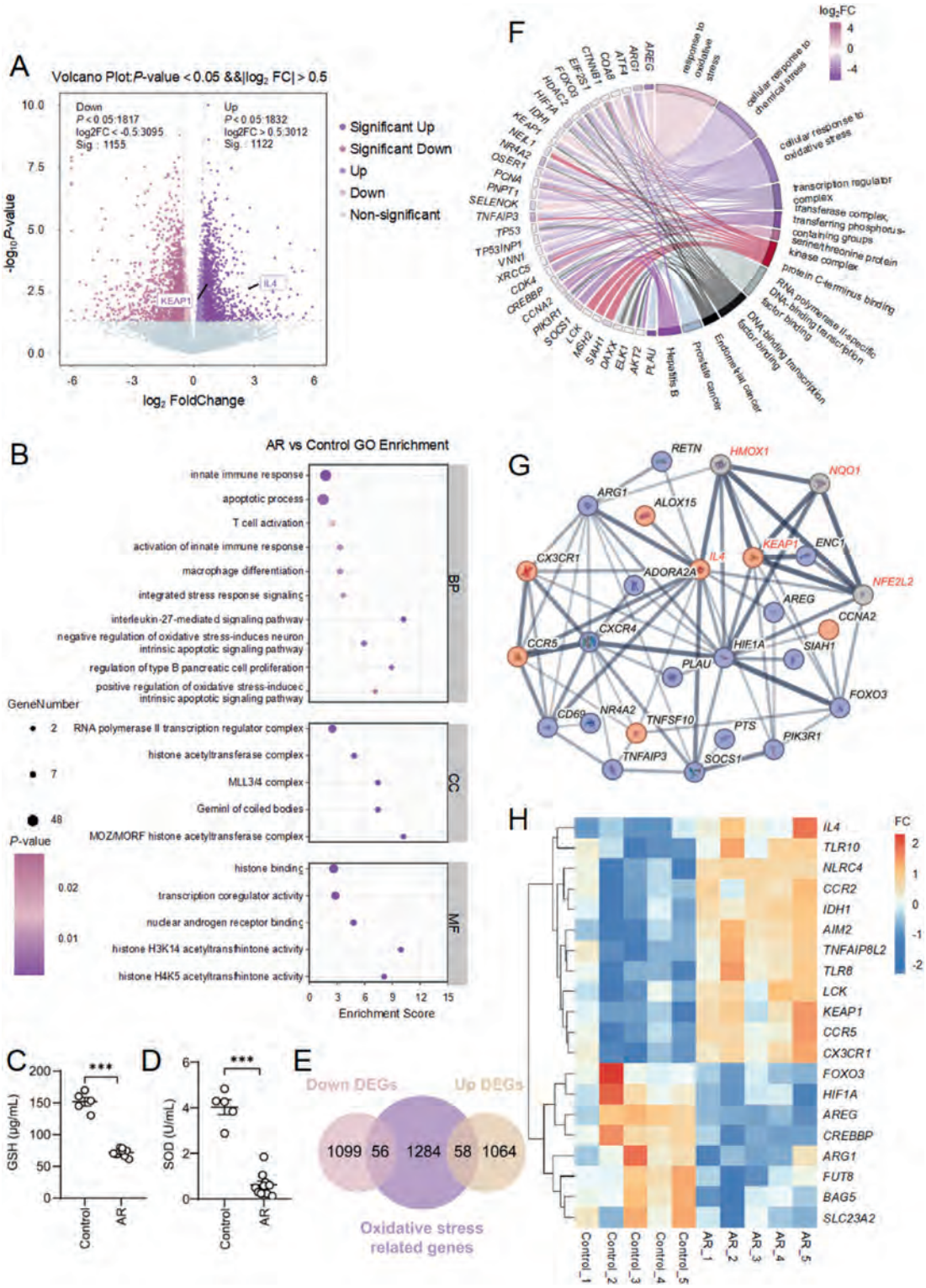

Figure 5 KEAP1-related oxidative stress and inflammation are dysregulated in the PBMC or NALF of AR patients. (A) The volcano plot of individual genes between AR patients ($n = 5$) and control participants ($n = 5$). The cutoff value is set as $P < 0.05$ and $|\log_2 FC| > 0.5$. (B) GO term enrichment analysis for DEGs between AR patients and control participants. BP: biological process; CC: cellular component; MF: molecular function. (C, D) The concentrations of GSH (C) and SOD (D) in human NALFs determined by assay kits. $n = 5$ (control participants) and $n = 10$ (AR patients) biologically independent samples. (E) The Venn diagram shows the overlap between upregulated or downregulated DEGs (1122/1155 genes) and oxidative stress related genes (1398 genes) in the GO database. (F) The chord diagram shows the GO and KEGG term enrichment analysis for oxidative stress related DEGs ($P < 0.01$ and $|\log_2 FC| > 0.5$). (G) Integrated gene network using STRING showing interactions with oxidative stress related DEGs. Red/blue nodes represent upregulated/downregulated genes, and gray nodes represent other genes may strongly

intranasally treated with DEX were decreased. With the intranasal treatment of the homoPROTAC **8** (5, 10, 20 mg/kg), the allergic symptoms were alleviated apparently in a dose-dependent manner. Next, we evaluated the anti-inflammatory effects of the homoPROTAC. Results showed that the compound could dose-dependently decreased the level of TNF-α (Fig. 6D), IL-1β (Fig. 6E), IL-6 (Fig. 6F) and IL-4 (Fig. 6G) in the nasal lavage fluid (NALF) of the OVA-induced AR model. In addition, the serum levels of histamine (Fig. 6H), OVA-specific IgE (Fig. 6I) and IL-13 (Fig. 6J) were effectively alleviated. Moreover, flow cytometry analysis was employed to quantify the total infiltrating myeloid cells and eosinophils (Fig. 6K and L, Supporting Information Fig. S6A−S6C). The results demonstrated a significant reduction in both cell types following the chemical knockdown of Keap1.

Histological staining of Hematoxylin-Eosin (H&E), Giemsa and immunohistochemistry (IHC) clearly demonstrated that the homoPROTAC significantly reduced the histological damage of nasal mucosa caused by AR (Fig. 6M). H&E staining revealed pronounced nasal mucosal edema, epithelial damage, and secretory acinar hyperplasia in the OVA group compared to the control group (Fig. S6D). Notably, the histological lesions associated with the nasal mucosa inflammatory response were effectively mitigated by the homoPROTAC treatment, with a similar effect observed following treatment with DEX. Giemsa staining further corroborated the eosinophil infiltration within the nasal mucosa, which was more pronounced in the OVA group compared to the control group (Fig. S6E). In line with the flow cytometry results, eosinophil infiltration was significantly reduced after treatment with DEX or a high dose of **8**. In addition, IHC staining of $CD45^+$ cells provided a direct visualization of the changes observed in flow cytometry (Fig. S6F). Specifically, a marked increase in $CD45^+$ cells was evident in the OVA group compared to the control group, which was subsequently reduced upon treatment with DEX or a high dose of **8**. The GSH and SOD levels with treatments were accordingly regulated, confirming the anti-oxidative stress capacity of the homoPROTAC (Fig. S6G and S6H). These findings reinforce the chemical knockdown efficacy of the homoPROTAC in mitigating the inflammatory response within the nasal mucosa.

To further verify the effective chemical knockdown of Keap1 *in vivo*, we initially procured the nasal mucosa samples from the AR mouse model for mRNA-seq analysis. The comprehensive assessment encompassed the total number of DEGs and their expression levels across various conditions, including OVA versus Control, three doses of the homoPROTAC versus OVA, and DEX versus OVA, as presented in Supporting Information Fig. S7A and S7B. We delved into pathways involving *Keap1*, specifically "*Keap1−Nfe2l2*" (Fig. 6N−R) and "Nuclear events mediated by *Nfe2l2*" (Fig. S7C) were explored through the GSEA analysis. We observed a positive correlation between both pathways in the OVA group compared to the control group. Conversely, in the treatment groups, these pathways exhibited a negative correlation, with the disparity in the clustering of genes belonging to these two pathways becoming more pronounced as the drug dose escalated, when compared to the OVA group. The above results indicated that homoPROTAC-ing Keap1 *in vivo* indeed affected the phenotype of the AR mouse model by regulating the Keap1−Nrf2 pathway. We further screened and displayed AR related inflammatory factors and transcription factors with significant differences in both pathways generating a heatmap (Fig. 6S). Consistently, we observed that the inflammatory factors such as *Il4*, *Il6*, *Muc5ac*, *Ccl5*, *Ccl11*, *Ccr2*, *Ccr5* and *Tslp* were downregulated following treatment with **8**, which were upregulated in the OVA group compared to the control group. Next, we performed Western blot assay using nasal mucosa samples from the AR mouse model (Fig. 6T and Fig. S7D). After treatment with 8, the OVA-induced AR mice showed a significant decrease in Keap1 expression in nasal mucosa (Fig. 6U). Conversely, there was an increase in the expression of downstream factors including HO-1 (Fig. 6V) and NQO1 (Fig. 6W), suggesting the activation of Keap1-mediated signaling pathways. In summary, our findings demonstrate that intranasal administration of the homoPROTAC effectively induces a chemical knockout of Keap1 in the nasal mucosa, thereby providing a promising therapeutic approach for mitigating inflammation and oxidative stress in the nasal mucosa of AR mice.

3. Discussion

We have successfully developed and demonstrated a proof-of-concept for the self-degradation of Keap1 as a homoPROTAC-mediated approach for treating AR. Our findings reveal that the homobivalent molecules, designed to efficiently dimerize the Keap1 E3 ubiquitin ligase, can induce substantial degradation of Keap1 protein at nanomolar concentrations. Through first characterizations of ternary complexes of $(Keap1)_2$:$(homoPROTAC)_1$, we have confirmed the underlying binding mechanism. These bivalents effectively target and degrade Keap1 in a wide range of cell types *via* an ubiquitin−proteasomal pathway, demonstrating their broad applicability. Notably, the homoPROTAC exhibits remarkable potency in degrading Keap1 in HNEpCs and significantly anti-inflammatory effects. Furthermore, we have observed dysregulation of Keap1-related oxidative stress and inflammation in clinical AR patients, underscoring the biological significance of Keap1 and its role in AR. Encouragingly, we have employed our novel homoPROTAC^{KEAP1} molecule in an AR mouse model and validated the efficacy in managing AR symptoms, oxidative stress and inflammation, as well as the ability to regulate gene expression through mRNA-seq analysis. To our knowledge, it is an unprecedented achievement in leveraging a novel chemical knockdown technology to induce the self-degradation of Keap1 protein for homoPROTAC-ing AR treatment.

Targeted protein degradation (TPD) represents an innovative chemical knockdown approach that harnesses the intricate machinery of the ubiquitin−proteasomal system to selectively degrade specific proteins of therapeutic interest[44,45]. This strategy offers a precise and potent means of modulating protein levels within cells, thereby eliciting desired therapeutic effects[46]. In 2018, Jiang's group[47] validated the recruitment capability of Keap1 as a ubiquitin E3 ligase through a PROTAC-mediated Tau protein degradation. In 2022, Gray group expanded this approach to demonstrate the recruitment

associate with *KEAP1* or *IL4*. The thickness of the line represents the interaction score (minimum required interaction score = 0.4). (H) The heatmap of oxidative stress related DEGs representatively between AR patients and control participants. Red/blue nodes represent upregulated/downregulated genes. Results are expressed as the mean ± SEM. $***P < 0.001$.

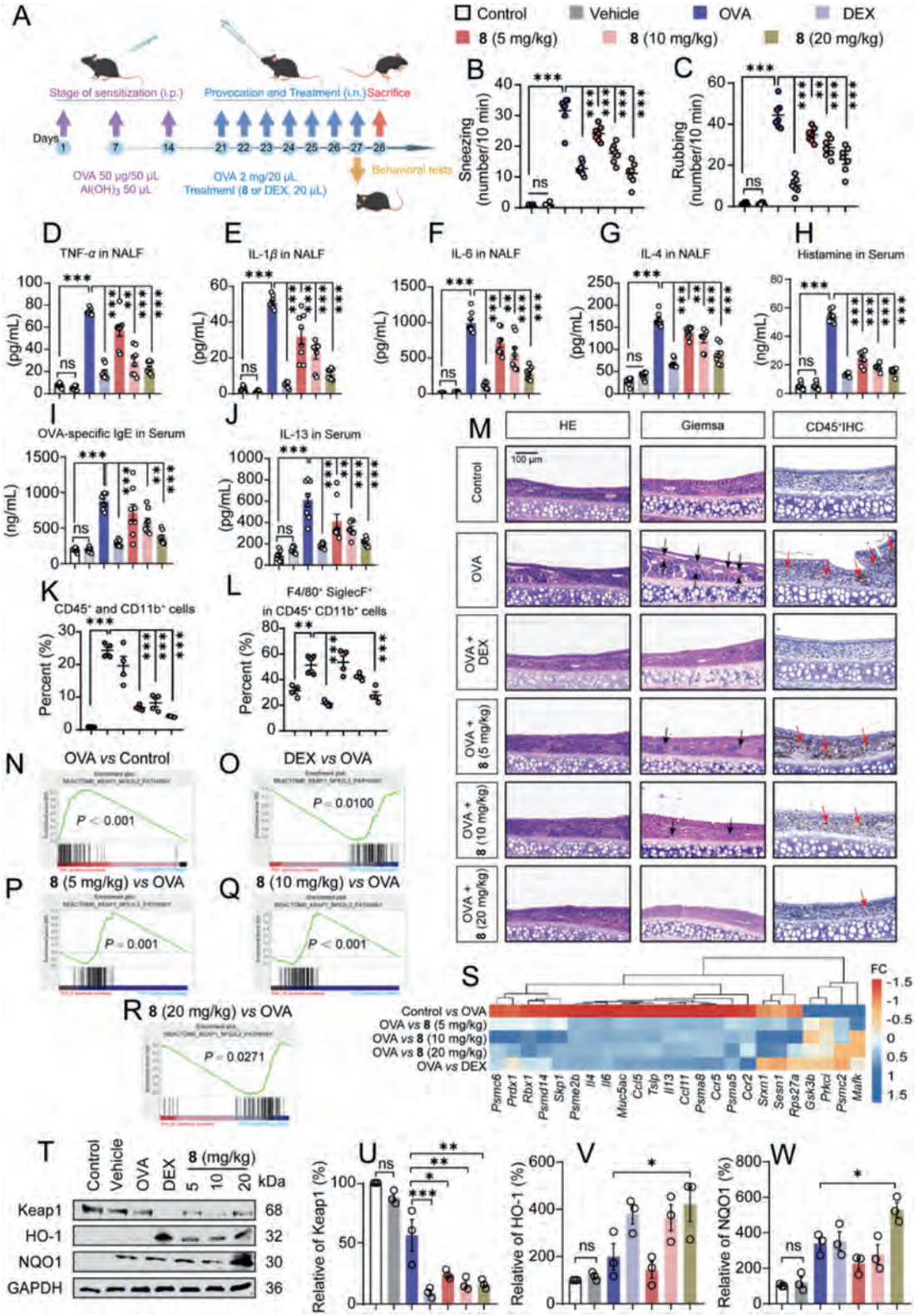

Figure 6 The homoPROTAC mitigates allergic nasal inflammation by regulating Keap1−Nrf2 pathway in the OVA-induced AR mouse model. (A) Schematic illustration of constructing the OVA-induced AR mouse model, the schedule of treatment and the administration methods. i.p., intraperitoneal injection; i.n., intranasal administration. (B) Behavior analysis showing frequency of sneezing of mice ($n = 8$). (C) Behavior analysis showing frequency of rubbing of mice ($n = 8$). (D−G) The concentrations of nasal mucosal inflammatory factors including TNF-α (D), IL-1β (E), IL-6 (F), IL-4 (G) in NALF determined by ELISA ($n = 8$). (H−J) The concentrations of histamine (H), OVA-specific IgE (I), IL-13 (J) in serum were determined by ELISA ($n = 8$). (K, L) The changes of inflammatory myeloid cells ($CD45^+$ $CD11b^+$) and eosinophils ($CD45^+$ $CD11b^+$ $F4/80^+$ $SiglecF^+$) in mouse nasal mucosa determined by flow cytometry. $n = 4$ biologically independent samples. (M) Evaluation of the

handling for various targets, including BET family proteins and murine focal adhesion kinase (FAK)[48]. Despite these advancements, the degradation scope of Keap1 remains relatively narrow, which is dominantly degraded by cereblon (CRBN)-linked PROTACs[48]. Nevertheless, ongoing research into Keap1-related PROTACs utilizing diverse Keap1 ligands has led to enhanced degradation efficacy, showcasing positive results across multiple cell and animal models[40,49-54]. Notably, while the degradation of Keap1 remains limited, its utility as an E3 ligase for targeting other proteins of interest underscores its significant potential in TPD strategies. The Jiang group obtained bivalent Keap1 inhibitors because of analyzing the mechanism on homodimerization of Keap1 with Nrf2[34]. Since the bivalent inhibitor **J3** was not designed based on the E3 ligase characteristics of Keap1, we further verified that it did not exhibit degradation behavior like compound **8** (Fig. S7E). On the basis of our crystallography studies, we obtained the dimerization of Keap1 protein and we have validated our hypothesis by designing a bivalent homoPROTAC^{KEAP1} construct to occupy the pocket of the dimer (Fig. 1A). This innovative approach achieved chemical knockdown of Keap1, embodying the concept of "self-destruction" of a protein. This strategy has been successfully explored in limited E3 systems, including CRBN[55], von Hippel-Lindau (VHL)[38,56], and murine double minute-2 (MDM2)[57,58]. More recently, Junk et al.[59] have further advanced this field by introducing a novel homo-bacPROTAC system, demonstrating its effectiveness in self-degrading the mycobacterial protease complex, specifically targeting the ClpC1 and ClpP1P2 protein subunits. Herein, we embarked on an exploration of different linkers based on our previous Keap1 inhibitors and screened out compound **8**, featuring a PEG linker, as the optimal binder to Keap1 and the most potent degrader in a Keap1-overexpressing cell line. Most pronouncedly, our crystallographic analyses unveiled the pioneering ternary complex of Keap1 protein with homoPROTACs, offering invaluable structural insights that pave the way for further modification.

Extending our investigations, we discovered that this degradation effect was profound, manifesting across multiple cell lines, including human nasal mucosa epithelial cells. Remarkably, this chemical-induced degradation mirrored the biological knockdown of Keap1, triggering its self-destruction. The advantage is obvious: more efficient and therapeutic. Our current research endeavors are centered on elucidating the intricacies of oxidative stress. Leveraging the meticulous collection of clinical samples, we conducted a comprehensive analysis of a gene expression profile related to AR. We found striking dysregulations within the Keap1-associated oxidative stress and inflammatory pathways in human PBMCs and NALFs, suggesting a pivotal role in AR pathogenesis. To further validate these findings, we delved into the nasal mucosa samples derived from the OVA-induced AR mouse model. Employing the mRNA-seq analysis, we corroborated the alterations in the "*Keap1−Nfe2l2*" and "Nuclear events mediated by *Nfe2l2*" pathways. These discoveries underscore the intricate interplay between oxidative stress, and inflammation in the context of human AR, offering fresh insights into potential therapeutic direction for this prevalent condition. Of particular significance, intranasal administration of the homoPROTAC in an OVA-induced AR mouse model yielded exceptional efficacy. The treatment effectively reduced inflammatory markers such as IL-4 and IL-6, while upregulating the expression of downstream factors HO-1 and NQO1, highlighting its potent immunomodulatory capabilities.

At present, the treatment of AR mainly falls into three categories: hormone therapy, targeted drug therapy, and immunotherapy[10]. Hormones such as dexamethasone can only control symptoms in the short term, and prolonged use may lead to systemic side effects. The targeted drugs are in a stage of vigorous development. However, the effect of many targets is uncertain, and the cost is high. Immunotherapy, a radical treatment method, requires continuous stimulation with gradient allergens over a long period (at least half a year or more). Although there is a possibility of cure, it is time-consuming and costly. Moreover, these three methods involve the use of systemic drugs, and the side effects are not conclusive. In particular, immunotherapy may stimulate systemic allergies, posing a risk. Chemical knockdown compounds are designed based on specific targets, utilizing the endogenous ubiquitin−proteasome pathway to achieve the same efficacy as biological knockdown. This innovative molecule effectively induces homodimerization of Keap1, triggering its proteasomal-dependent "self-destruction" across multiple cell types. In animal experiments, no side effects were demonstrated even at high doses, making them safe and reliable.

It is important to acknowledge potential limitations in our investigation. Firstly, the dimerization of the 1,4-diaminonaphthalene scaffold, which tightly occupies the binding pocket with a high affinity, inherently results in a high molecular weight. This, however, beyond the five principles of drug-likeness, potentially compromises critical physicochemical properties such as solubility, bioavailability, and *in vivo* pharmacodynamic performance. Notably, our prior endeavors to asymmetrically optimize one side of the benzosulfamide structure have yielded active inhibitors, exhibiting enhanced bioavailability and solubility[31,35,36,60,61]. Consequently, for the high-molecular-weight compounds, intranasal administration may represent a viable route to achieve satisfactory *in vivo* efficacy. Our present studies delineate potential strategies forward and highlight opportunities for synthesizing the next generation of homoPROTACs for attempting diverse administration routes. Secondly, the most prominent inflammatory features of AR are

histological damage of nasal mucosa analyses with H&E, Giemsa and IHC staining of nasal mucosa in different conditions. Scale bar = 100 μm. Black arrow points to the representative cytoplasmic red stained eosinophils in the Giemsa staining; red arrow points to the representative CD45$^+$ cells in IHC staining (n = 3). (N−R) GSEA plots for the "Keap1−Nfe2l2" pathway under different conditions. (S) The heatmap shows the representatively different expressions of "Keap1−Nfe2l2" pathway related genes and AR related inflammatory genes. (T−W) Effect of the homoPROTAC on Keap1 *in vivo*, as well as the subsequent changes in downstream gene expressions (HO-1 and NQO1), and the gray-scale analysis. (n = 3). Control, control group; OVA, ovalbumin-induced AR mouse model group; Vehicle, control mouse treated with the solvent of compound **8** (including 5% DMSO, 45% PEG400, 50% PBS); DEX, OVA-induced mouse model treated with DEX (1 mg/kg/mouse); **8** (5), the OVA-induced mouse model treated with compound **8** (5 mg/kg/mouse); **8** (10) the OVA-induced mouse model treated with compound **8** (10 mg/kg/mouse); **8** (20), the OVA-induced mouse model treated with compound **8** (20 mg/kg/mouse). Data was expressed as the mean ± SEM. ns, $P \geq 0.05$; *$P < 0.05$; **$P < 0.01$; ***$P < 0.001$.

localized within the nasal cavity[62,63]. Transcriptome sequencing of human PBMCs collected in this study cannot fully elucidate all biological information related to AR progression, particularly the transcriptional changes occurring in the nasal mucosal epithelium, which may serve as the initial site for oxidative stress and inflammation. The AR patients enrolled in our study exhibited overt symptoms accompanied by markedly elevated IgE levels in peripheral blood, rendering their PBMCs particularly representative of the body's regulatory response to AR-induced oxidative stress and inflammation. To delve deeper into their potential contributions, we conducted an intersection screening using the oxidative stress-related gene set from the GO database alongside the DEGs. However, to attain a more precise portrayal, collecting human nasal mucosa tissues for single-cell RNA sequencing (scRNA-seq) or nuclear RNA sequencing (snRNA-seq) would undoubtedly provide invaluable insights. Thirdly, we have comprehensively validated the homoPROTAC through an SEC assay, which demonstrated the successful formation of a ternary complex comprising two molecules of Keap1 protein and one molecule of the homoPROTAC. Furthermore, our crystallographic experiments confirmed the structural integrity and interaction pattern of this complex, providing strong evidence for the functionality and specificity of our homoPROTAC design. The degradation efficacy of the homoPROTAC within cells has been thoroughly validated, whereas the precise molecular recruitment process that occurs within these cells remains to be fully elucidated, such as using overexpressed fluorescent-labeled Keap1 proteins.

In conclusion, we have successfully designed and synthesized the first example of HomoPROTAC^{KEAP1} for the AR treatment. The homoPROTAC exhibits promising activity in alleviating AR-related symptoms, inhibiting Keap1-mediated oxidative stress, and alleviating the inflammation in the AR mouse model. Our findings highlight the potential of chemical knockdown of Keap1 *via* a homoPROTAC technology as an innovative and promising therapeutic strategy for addressing AR disorders.

4. Experimental

4.1. Chemistry

All starting materials were obtained from commercial sources and were analytically pure. The ^{1}H NMR and ^{13}C NMR spectra were recorded on Bruker Avance 500 and 600 MHz spectrometers (Bruker Company, Germany) using tetramethylsilane as an internal standard and DMSO-d_6 as solvents. Chemical shifts (δ values) and coupling constants (J values) are given in ppm and hertz (Hz), respectively. MS data were acquired using a quadrupole time-of-flight micro mass spectrometer. Thin-layer chromatography (TLC) analyses were carried out on silica gel plates HGF254 (Qingdao Haiyang Chemical, China). Column chromatography separations were carried out on a silica gel 200−300 mesh. The purities of the compounds were analyzed by HPLC (Shimadzu CTO-20A) using a C18 column (YMC-Pack ODS-A, S-5 μm, 250 mm × 10.0 mm I.D.) with 90% methanol/10% water as the mobile phase at a flow rate of 2 mL/min, and all final compounds exhibited purities greater than 95%. Procedures for the preparation and chemical characterizations of the final compounds are described in Supporting Information.

4.1.1. Recombinant protein expression and purification

Genes coding human Keap1 Kelch domain (residues 322-609, E540A, E542A) was subcloned into pET28a with a N-terminal, thrombin protease-cleavable His_6-tag and expressed in *Escherichia coli*. Arctic Express™ (DE3). The cells were grown at 37 °C/220 rpm to an approximate OD_{600} of ∼0.8 before induced with 0.25 mmol/L β-D-thiogalactopyranoside (IPTG). After 20 h at 16 °C/220 rpm, the cells were harvested, resuspended in lysis buffer containing 20 mmol/L Tris-HCl (pH 8.0), 300 mmol/L NaCl and 1 mmol/L DTT and lysed using a French press with two passes at 15,000 p.s.i. Cell debris was removed by centrifugation. Then, the supernatant was loaded onto a Ni^{2+}-NTA affinity column (Smart Lifesciences). After competitive wash with 20 mmol/L Tris-HCl (pH 8.0), 300 mmol/L NaCl, 25 mmol/L imidazole, the protein was eluted from the column using 20 mmol/L Tris-HCl (pH 8.0), 300 mmol/L NaCl and 250 mmol/L imidazole. The eluted His_6-Keap1 Kelch domain protein was further purified by cleaving the His_6-tag with thrombin protease and loaded onto a Hiload 16/600 Superdex 200 pg column (Cytiva) pre-equilibrated with gel filtration buffer of 20 mmol/L Tris (pH 8.0), 300 mmol/L NaCl. The fractions of the protein peaks were evaluated by reducing StainFree SDS-PAGE gel electrophoresis (Bio-Rad) and concentrated to 20 mg/mL using MWCO spin concentrator (Millipore) of 30 kDa, and then snap frozen in liquid N_2 for storage at −80 °C.

4.1.2. Fluorescence anisotropy assay

Determination of equilibrium dissociation constants K_{D2} for each compound was performed using the fluorescence anisotropy assay. FITC-βAla-DEETGEF-OH was applied as a competitive fluorescence probe and the binding affinity was characterized as K_{D1}. The binding affinity of the compounds to Keap1 was read using a SpectraMax M5 microplate reader in a buffer containing 50 mmol/L HEPES (pH 7.0), 150 mmol/L NaCl, and 1 mmol/L 1,4-dithiosonitol (DTT) with 485 nm excitation and 535 nm emission after 60 min incubation at room temperature. The final concentration of the protein was 10 nmol/L, the final concentration of the probe was 10 nmol/L, and the compounds were half diluted from 50 μmol/L in sequence.

4.1.3. Microscale thermophoresis assay

The His-tagged Keap1 was labeled with RED-tris-NTA dye (Nanotemper technologies, MO-L018) and the fluorescence values were measured with microthermometers (Nanotemper technologies, MO-K022-SP) in buffer solution containing 1 × phosphate buffered saline (PBS, pH 7.2−7.4) and 0.05% Tween-20 after 30 min incubation at room temperature. The final concentration of the labeled protein was 5 nmol/L and the compounds were half diluted from 12.5 μmol/L in sequence.

4.1.4. Size-exclusion chromatography

The SEC experiments were carried out in a ÄKTA pure system (Cytiva) at room temperature. The oligomeric state of the Keap1−compound complex in solution was analyzed by gel filtration in a buffer containing 20 mmol/L Tris-HCl (pH 8.0), 300 mmol/L NaCl, and 1 mmol/L DTT using a Superdex 200 Increase 10/300 GL column (Cytiva) calibrated with globular proteins of known molecular weight (Cytiva, 28-4038-42). Keap1 protein (14 μmol/L) was incubated with compounds in different concentrations or DMSO (<1%) for 1 h at room temperature prior to injection. Sample volume for each injection was 500 μL, and

the flow rate was 0.6 mL/min. Peak elution was monitored using UV absorbance at 280 nm.

4.1.5. Crystallization

The protein was pre-incubated with the compounds on ice at a molar ratio of 2:1 for 30 min, and the samples were then subjected to crystallization using the sitting-drop vapor diffusion method. The Keap1: compound crystals were grown in 3.8 mol/L ammonium acetate, 0.1 mol/L HEPEs (pH 7.0) at 20 °C, then soaked in a cryo-protectant (reservoir solution supplemented with 30% (*v*/*v*) glycerol) and flash-frozen in liquid nitrogen before data collection.

4.1.6. Data collection and structure determination

X-ray diffraction data were collected at BL02U1 and BL19U1 beamline of Shanghai Synchrotron Radiation Facility and processed using program XDS. The structure was solved through molecular replacement using Phaser-MR in program PHENIX. The structure refinement was carried out using PHENIX, and manual model building with Coot. All the crystallographic information is summarized in Table S1.

4.1.7. Cell culture and treatment

MDA-MB-231, HEK293T, HNEpC, Beas-2B, LLC and RAW264.7 were propagated in DMEM supplemented with 10% fetal bovine serum (FBS) (Bio-Channel, BC-SE-FBS08) and 100 μg/mL of penicillin/streptomycin (Biochannel, BC-CE-007) at 37 °C and 5% CO_2. Culture medium was changed three times a week, depending on cell density, and cells were passaged for further cultivation or differentiation experiment at 80%−90% confluency. For passaging, cells were trypsinized using 0.05% Trypsin/EDTA (Biochannel, BC-CE-002) during 1−2 min, washed in medium. For compound treatment experiments, cells were treated with compounds at the desired concentrations, reaching final DMSO concentration of 0.1% (*v*/*v*). Cells were incubated for the desired time before harvesting. For mechanism verification, Beas-2B, LLC, RAW264.7, AML-12, and HNEpC cells were pretreated with MG132 (CAS#133407-82-6, Targetmol, USA) and MLN4924 (CAS#905579-51-3, Targetmol, USA). The bivalent inhibitor **J3** (The original code is compound **3** in the reference paper[34]) was kindly provided by Prof. Zhengyu Jiang. MLN4924 was added into the desired wells at 0.3 μmol/L as a final concentration, MG132 was added into the desired wells at 0.1 μmol/L as a final concentration, containing 0.1% (*v*/*v*) of DMSO. MG132 or MLN4924 was treated the cells for 3 h before the compound treatment. After that, the desired wells were treated with compound **8** containing 0.1% (*v*/*v*) DMSO.

4.1.8. Establishment of stable cell lines

Lentivirus of KEAP1 (NM_203500.2, Target Seq: GTGGCGAATGATCACAGCAAT) was purchased from Obio Technology (Shanghai) Corp., Ltd. MDA-MB-231 and HNEpC cells were infected with the corresponding lentiviruses for 16−24 h. After 72 h, Keap1-KD cell lines were selected using puromycin (1 μg/mL) for additional 72 h. LLC KO cells were purchased from Cyagen (SY-KO-00161).

4.1.9. Acquisition of cell protein extracts

Cells were seeded in 6-well plates with either 3×10^5 or 5×10^5 cells per well in 2 mL of medium. After the compound stimulation, the supernatant was sucked away, the cells were washed with ice-cold PBS, and then the NP40 lysis buffer (Beyotime, ST2045) containing 1% (*v*/*v*) of protease&phosphatase&PMSF inhibitor (Weiaobio, WB0122) was added. For protein extracts, the dishes were placed on ice for 15 min. The cell lysate was collected and centrifuged at 20,000×*g* at 4 °C for 5 min. The protein concentration of the supernatant was measured with a BCA Protein Assay Kit (Biosharp, BL521A) and then added 5 × loading buffer into the sample and store at −80 °C for future use.

4.1.10. Immunoblotting

Protein extracts were separated by SDS-PAGE on 10%−15% polyacrylamide gels and transferred to a nitrocellulose (NC) membrane (Millipore) using electro-transfer. The NC membrane containing the proteins was blocked with 5% skim milk at room temperature for 1 h. The blocking solution was removed by aspiration, and the membrane was washed 3 times with the PBS containing 0.1% Tween-20 (PBST), for 5 min/time. Then, the diluted primary antibody was immediately added. The membrane was incubated overnight at 4 °C. Primary antibodies included anti-human Keap1 (Santa Cruz, sc-365626); anti-mouse Keap1 (Cell Signaling Technology, D6B12), anti-Nrf2 (Proteintech, 80593-1-RR), anti-HO-1 (Proteintech, 10701-1-AP), anti-NQO1 (Abcam, ab34173), anti-Lamin B (Proteintech, 12987-1-AP) and anti-GAPDH (Proteintech, 60004-1-Ig). The primary antibodies were removed by aspiration, and the membrane was washed 3 times with the PBST, for 5 min/time. Then, the diluted secondary antibody was immediately added and the membrane was incubated at room temperature for 1 h. Fluorescent secondary antibody included Goat anti-Mouse IgG H&L (IRDye® 800CW, ab216772) and Goat anti-Rabbit IgG H&L (IRDye® 800CW, ab216773). The secondary antibodies were removed by aspiration, and the membrane was washed 3 times with the PBST, for 5 min/time. Images were photographed with Odyssey system (Li-Cor Biosciences) and then analyzed with Image J software.

4.1.11. Co-IP assay

To prepare whole-cell lysates, HNEpC cells were washed with precooled PBS, and then NP40 lysis buffer with 1% (*v*/*v*) of protease&phosphatase&PMSF inhibitor (Weiaobio, WB0122) was added to lyse the cells. After centrifugation for 15 min at 20,000×*g* under 4 °C, the supernatant was isolated for subsequent experiments. The protein concentration was confirmed by a BCA assay kit. Cell lysates were incubated with the indicated antibodies (Santa Cruz, sc-365626) on a shaker at 4 °C for 24 h. Next, protein L magnetic beads (MedChemExpress, HY-K0205) were added and incubated overnight at 4 °C. After washing three times with precooled PBST (1 × PBS + 0.5% Tween-20, pH 7.4), 1 × SDS-PAGE loading buffer was added. The mixture was then boiled at 95 °C for 5 min. Finally, immunoblot analysis was used to assess protein level. Primary antibodies included anti-human Keap1 (Santa Cruz, sc-365626), anti-ubiquitin (Proteintech, 10201-2-AP), and anti-GAPDH (Proteintech, 60004-1-Ig). Fluorescent secondary antibody included Goat anti-Mouse IgG H&L (IRDye® 800CW, ab216772) and Goat anti-Rabbit IgG H&L (IRDye® 800CW, ab216773).

4.1.12. Electrophoretic mobility shift assay (EMSA)

To prepare nucleus-cell lysates, the HNEpC cells were washed with precooled PBS, and then nuclear extraction lysis buffer (Minute™ Cytoplasmic and Nuclear Extraction Kits for Cells,

Invent Biotechnologies, SC-003) with 1% (*v*/*v*) of protease&-phosphatase&PMSF inhibitor (Weiaobio, WB0122) was added to lyse the cells. After centrifugation for 15 min at 20,000×*g* under 4 °C, the supernatant was isolated for subsequent experiments. The protein concentration was confirmed by a BCA assay kit. Then, according to the chemiluminescence EMSA kit (Beyotime Biotechnology, GS009), the preparation of EMSA PAGE Gel, the binding reaction with the probe, electrophoresis, film transfer, cross-linking and detection were carried out. Finally, the image was developed by automatic chemiluminescence image analysis system (Tanon Chemi Dog 5200T, China).

4.1.13. Immunofluorescence staining

The cell crawling tablets were prepared after the compound treatment, washed with PBS, fixed with 4% paraformaldehyde for 10 min, washed with PBS, incubated with 0.1%Triton X-100 for 10 min, washed with PBS, and sealed with 5% BSA for 1 h. The primary antibody was diluted in appropriate proportions and incubated at 4 °C overnight, and the secondary antibody was incubated at room temperature for 1 h away from light after washing with PBS with fluorescent labeling. The nucleus was stained with DAPI (Beyotime, C1002), and then the film was sealed with an anti-fluorescence quenching sealing agent. Finally, the film was observed and photographed under a fluorescence microscope. Attention was paid to avoiding light and preventing sample drying during the whole operation, and the operation was strictly carried out in accordance with the antibody instructions. Primary antibodies included anti-human Keap1 (Santa Cruz, sc-365626), and anti-Ubiquitin (Proteintech, 10201-2-AP). Fluorescent secondary antibody included Goat anti-Mouse IgG H&L (Alexa Fluor® 488, ab150113) and Goat anti-Rabbit IgG H&L (Alexa Fluor® 568, ab175471).

4.1.14. Anti-inflammatory experiment

HNEpC cells were seeded in 96-well plates with 1×10^4 cells per well in 200 μL medium in order to achieve 80% confluence at 37 °C and 5% CO_2. Two treatment strategies (pre- and co-treatments) were performed to evaluate the anti-inflammatory activity of the target compounds. Pre-treatment: Compound **8** (10 μmol/L) was administered and pre-treated the cells for 19.5 h at first. Then, the cells were challenged by LPS (200 ng/mL) for another 4.5 h, and papain (10 μg/mL) stimulated the cells for 0.5 h before harvesting the supernatant[42]. Co-treatment: LPS (200 ng/mL) mixed with compound **8** (10 μmol/L) and then were added to the cells. After 4 h, papain (10 μg/mL) was added. Plates were subsequently incubated for another 20 h before harvesting the supernatant. NXPZ-2 (10 μmol/L) was used as a comparison. TNF-α and IL-6 in cell supernatant were determined using a human TNF-α ELISA kit (Invitrogen, 88-7346-88) and a human IL-6 ELISA kit (Invitrogen, 88-7066-88), and measured by SpectraMax M5 (USA) with 450 nm. RAW264.7 cells were seeded in 96-well plates with 1×10^5 cells per well in 200 μL medium in order to achieve 80% confluence at 37 °C and 5% CO_2. LPS (1 μg/mL) mixed with compound **8** (10 μmol/L) and then were added to the cells. Plates were subsequently incubated for different period of time points before harvesting the supernatant to detecting different factors. NXPZ-2 (10 μmol/L) was used as a comparison. The concentrations of mouse TNF-α and IL-6 were determined by ELISA kits (Invitrogen, 88-7324-88, and 88-7064-88). The concentration of NO was determined by a kit (Beyotime, S0021S).

4.2. Animals

Six-week-old C57BL/6 male wild-type mice were purchased from Shanghai BK/KY Biotechnology Co., Ltd. Animals were assigned randomly through a table of random numbers to cohorts by a technician that was blinded to the appearance or other characteristics of the animals. All animal experiments were undertaken in accordance with the National Institute of Health Guide for the Care and Use of Laboratory Animals, with the approval of the Animal Care and Use Committee of Naval Medical University, Shanghai, China (Approval No.: 82022065). All animals were housed in a virus-free facility and maintained in a standard temperature of 21−23 °C with relative humidity of 35%−65% and light controlled (12 h light/dark) animal facility.

4.2.1. The OVA-induced AR mouse model

The OVA-induced AR mice model was constructed as our previously description[64]. In sensitization stage, mice were intraperitoneal injected with a mixture (1:1) of OVA (1 μg/mL, Sangon, CAS#9006-59-1)/PBS and Imject™ Alum Adjuvant (Invitrogen, 77161) once every week for 3 weeks. In stimulation stage, mice were intranasally challenged with OVA (2 mg/20 μL) or PBS (20 μL) every day for 7 consecutive days. In addition, compound **8** dissolved in the solution including 5% DMSO, 45% PEG and 50% PBS was used to administer intranasal adjuvant challenge to mice (0, 5, 10, 20 mg/kg) each once a day for 7 consecutive days 6 h before OVA challenging. 10 min after each nasal challenge with OVA, the frequency of sneeze and rubbing were counted in a blinded manner for 10 min. Sneezing was defined as an explosive expiration promptly following a deep inspiration, while rubbing was defined as perinasal scratching with one or both forelimbs.

4.2.2. Tissue and blood sampling

The respiratory nasal mucosal tissues of the OVA-induced AR mouse model were harvested and subjected flow cytometry, Western blotting and oxidative stress related kit (GSH, Boxbio, AKPR008M and SOD, Boxbio, AKAO001M) detection. NALF subjected to ELISA was collected by perfusing PBS from the trachea into the nasal cavity, with 1 mL/mouse. Serum subjected to ELISA was prepared through centrifugation of peripheral blood collected from the inferior vena cava, after 24 h following the last nasal challenge. Concentrations of TNF-α, IL-1β, and IL-6 were determined by ELISA Kit (Invitrogen, 88-7324-88, 88-7013-88, and 88-7064-88).

4.2.3. Flow cytometry analysis

Briefly, the nasal mucosa tissues from mice were minced into small pieces in complete RPMI 1640 medium containing 1 mg/mL DNase I (Servicebio, G3342), 500 U/mL collagenase I (Servicebio, GC305013) and 250 U/mL hyaluronidase (Sangon Biotech, A005477) for 1 h at 37 °C. The single cell suspension was then collected by centrifugation. Subsequently, cells were fixed in 4% paraformaldehyde (Servicebio, G1101-3 ML) and stained with fluorescent-conjugated antibodies including BV711 anti-mouse CD45 (Biolegend, 103147), FITC anti-rat CD11b (BD Biosciences, 557396), FITC anti-mouse F4/80 (Biolegend, 123108) and PE/Cyanine7 anti-mouse Siglec-F (Biolegend, 155528). The myeloid cells were identified as $CD45^+$ $CD11b^+$, and eosinophils were defined as $CD45^+$ $CD11b^+$ $F4/80^+$ $SiglecF^+$. After performing flow cytometric analysis on BD

Fortessa flow cytometer (BD Biosciences), the data were analyzed using FlowJo_v10.8.1 software.

4.2.4. Histological and immunohistochemistry staining

The sinonasal cavity structure of the OVA-induced mouse model was fixed in 4% paraformaldehyde and embedded in paraffin for further histologic and immunologic analysis. For histopathological analysis of mouse nasal tissues, the dewaxed 6 μm tissue sections were stained with H&E and Giemsa. For immunohistochemistry staining, the sections were incubated with anti-CD45, (Biolegend, 103147) diluted 1:200 in PBS containing 4% bovine serum albumin at 4 °C overnight. On the next day, immunostaining was performed using Dako ChemMate EnVision Detection Kit Peroxidase/Diaminobenzidine (DAB) Rabbit/Mouse (Dako, Glostrup, Denmark), which resulted in a brown-colored precipitate at the antigen site. Subsequently, sections were counterstained with hematoxylin. The images were captured using an Olympus BX53 microscope. The individual that performed this analysis was blind to the groups of the experiment.

4.3. Human samples

This study was conducted in accordance with the guidelines by the Medical Ethics Committee of Shanghai Changzheng Hospital (No. 2023SL076A). A total of 10 AR patients and 5 control participants involved in this study were from the Department of Otolaryngology, Shanghai Changzheng Hospital. The diagnosis of AR was made according to the international consensus statement published in 2023[65]. In detail, the AR patients included in our study met the following criteria: 1. Aged 18−65 years old. 2. Presenting with typical symptoms of AR, including paroxysmal sneezing, clear rhinorrhea, nasal congestion, and nasal itching, often accompanied by ocular itching, tearing, redness, and a burning sensation. 3. Exhibiting typical signs of AR attacks, including pale and swollen nasal mucosa, swelling of the inferior turbinate, and abundant watery nasal secretions. 4. Positive skin prick test (SPT) results. Alternatively, serum evidence demonstrating sensitivity to at least one allergen. The control participants were matched with AR patients within the same age range but clinically did not meet the diagnostic criteria for AR and had no history of allergic diseases. All clinical information involved in this study including gender, age, medical history, and TNSS were obtained in outpatient service. The NALF was used to detected the concentration of GSH (Boxbio, AKPR008M) and SOD (Boxbio, AKAO001M) by kit. The IgE level in serum were measured by the Department of Clinical Laboratory, Shanghai Changzheng Hospital. PBMCs for mRNA sequencing were obtained by apheresis. Informed consent was obtained in accordance with the Declaration of Helsinki from every subject before the sample collection.

4.3.1. Transcriptomics study

The mRNA-seq was performed using human PBMC by OE Biotech Co., Ltd. (Shanghai, China), human nasal swabs by Novogene Co., Ltd. (Beijing, China) and mouse nasal mucosa by Shanghai Majorbio Bio-pharm Biotechnology Co., Ltd. (Shanghai, China). Total RNA was extracted from PBMC samples, nasal swab samples and mice nasal mucosa tissues using TRIzol reagent (Beyotime Biotechnology, China). RNA purity and quantification were evaluated by NanoDrop2000 spectrophotometer (Thermo Scientific, USA). RNA integrity was assessed using the Agilent 2100 Bioanalyzer (Agilent Technologies, Santa Clara, CA, USA). High-quality mRNA samples (human PBMC samples and mice nasal mucosa tissues: $OD_{260/280} = 1.8-2.2$, $OD_{260/230} \geq 2.0$, RIN $\geq$8.0, 28S:18S ≥ 1.0, >1 μg; human nasal swab samples: $OD_{260/280} = 1.8-2.2$, $OD_{260/230} \geq 2.0$, RIN $\geq$5.8, 28S:18S ≥ 1.0, >0.5 μg) were involved in a constructing sequencing library, comprising 10 PBMC samples (5 control participants and 5 AR patients), 15 nasal swab samples (5 control participants and 10 AR patients), and 18 mouse samples (3 mice in each group) that adhered to the established standards. The DEGs were evaluated using DESeq2. KEGG and GO term enrichment analysis were performed using online DAVID enrichment analysis service, and GSEA was performed using GSEA software. In addition, the gene interaction network was obtained by using online STRING database.

4.4. Statistical analysis

Unpaired two-tailed *t*-test was used for comparison of two groups, if the normality test was not passed the non-parametric Mann−Whitney test was used. One-Way ANOVA followed by Tukey's multiple comparison test was used for comparison of more than two groups, if normality test was not passed the non-parametric Kruskal−Wallis test was performed. The statistical significance level was set at 0.05, unless otherwise stated. All statistical analyses were performed with GraphPad Prism 8.

4.5. Associated content

Supporting Figures including repeated Western blots (Supporting Information Figs. 2, 3, 4, and 7), data collection and refinement statistics for crystal complex, experimental procedures for chemistry work, chemical characterizations of the target compounds (DOCX). Keap1 dimer (PDB code: 9J70), Keap1−compound **7** (PDB code: 9J71), Keap1−compound **8** (PDB code: 9J7G), Keap1−compound **1** (PDB code: 9J7F).

Acknowledgements

This work was funded by grants from the National Natural Science Foundation of China (U23A20439 and 82022065), Shanghai Shuguang Project (21SG38, China), Shanghai Chenguang Project, Shanghai Municipal Health Commission Project (2023Y0240, China), Shanghai Municipal Hospital Project (SHDC2023CRT003, China), Naval Medical University Project (2024QN032, China), and the "Zhuo Yue" Doctoral Student Training Program of Department of Pharmacy, Naval Medical University (2024ZY004, China). We thank Prof. Qian Zhang (National Key Laboratory of Medical Immunology, Institute of Immunology, Naval Medical University, Shanghai 200433, China) for providing LLC cells and LLC Keap1-KO cells. We thank Prof. Jin Hou (National Key Laboratory of Medical Immunology, Institute of Immunology, Naval Medical University, Shanghai 200433, China) for the data support in metatranscriptome sequencing in human nasal swab samples. We thank Prof. Yifan Ge (Associate Investigator at Chinese Academy of Sciences Shanghai, China) for providing the valuable discussion. We also thank Zhi-wen Cao, and Bo-jian Lin (Second Military Medical University) for the help of mouse model and treatment. We would like to thank staff members at SSRF BL19U1 for their technical assistance in X-ray diffraction data collection. In addition, we thank the staff members of the Large-scale Protein Preparation System (https://cstr.cn/31129.02.NFPS.LSPS) at the National

Facility for Protein Science in Shanghai (https://cstr.cn/31129.02.NFPS), for providing technical support and assistance in data collection and analysis. Fig. S4E and Fig. 6A were generated by Figdraw.

Author contributions

Chunlin Zhuang conceived and designed research; Jianyu Yan performed chemistry experiments; Jianyu Yan, Tianyu Wang, Ruizhi Yu, Hongming Shao, Tengfei Li, Zhe Wang and Xudong Cha performed biological experiments; Lijuan Xu and Ke Xu performed crystal experiments; Tianyu Wang and Huanhai Liu recruited patients and provided clinical sources; Jianyu Yan, Tianyu Wang, Lijuan Xu, Hongming Shao, Ke Xu, Zhenyuan Miao and Chunlin Zhuang analyzed data. Tianyu Wang, Tengfei Li, Xudong Cha and Zhe Wang performed clinical experiments; Jianyu Yan, Tianyu Wang, and Chunlin Zhuang wrote the manuscript. Xudong Cha, Chengguo Xing, Zhenyuan Miao, Ke Xu and Huanhai Liu discussed and edited the manuscript. Chunlin Zhuang and Huanhai Liu provided funding. All authors contributed with productive discussions and knowledge to the final version of this manuscript.

Conflicts of interest

The authors declare no conflicts of interest.

Appendix A. Supporting information

Supporting information to this article can be found online at https://doi.org/10.1016/j.apsb.2025.05.025.

References

1. Zhang Y, Zhang L. Increasing prevalence of allergic rhinitis in China. *Allergy Asthma Immunol Res* 2019;**11**:156−69.
2. Bernstein JA, Bernstein JS, Makol R, Ward S. Allergic rhinitis: a review. *JAMA* 2024;**331**:866−77.
3. Subspecialty Group of Rhinology, Editorial Board of Chinese Journal of Otorhinolaryngology Head Neck, Surgery Subspecialty Group of Rhinology, Society of Otorhinolaryngology Head Neck Surgery, Chinese Medical Association. [Chinese guideline for diagnosis and treatment of allergic rhinitis (2022, revision)]. *Chin J Otorhinolaryngol Head Neck Surg* 2022;**57**:106−29.
4. Asher MI, Montefort S, Björkstén B, Lai CKW, Strachan DP, Weiland SK, et al. Worldwide time trends in the prevalence of symptoms of asthma, allergic rhinoconjunctivitis, and eczema in childhood: ISAAC phases one and three repeat multicountry cross-sectional surveys. *Lancet* 2006;**368**:733−43.
5. Bousquet J, Khaltaev N, Cruz A, Denburg J, Fokkens WJ, Togias A, et al. Allergic rhinitis and its impact on asthma (ARIA) 2008 update (in collaboration with the World Health Organization, GA(2)LEN and AllerGen). *Allergy* 2008;**63**(Suppl 86):8−160.
6. Bousquet J, Cauwenberge PV, Khaltaev N, Group AW, Organization WH. Allergic rhinitis and its impact on asthma. *J Allergy Clin Immunol* 2001;**108**:S147−334.
7. Passali D, Cingi C, Staffa P, Passali F, Muluk NB, Bellussi ML. The international study of the allergic rhinitis survey: outcomes from 4 geographical regions. *Asia Pac Allergy* 2018;**8**:e7.
8. Hoyte FCL, Nelson HS. Recent advances in allergic rhinitis. *F1000Res* 2018;**7**:F1000.
9. Roxbury CR, Qiu M, Shargorodsky J, Woodard TD, Sindwani R, Lin SY. Association between rhinitis and depression in United States adults. *J Allergy Clin Immunol Pract* 2019;**7**:2013−20.
10. Bousquet J, Anto JM, Bachert C, Baiardini I, Bosnic-Anticevich S, Canonica GW, et al. Allergic rhinitis. *Nat Rev Dis Primers* 2020;**6**:95.
11. Alvaro-Lozano M, Akdis CA, Akdis M, Alviani C, Angier E, Arasi S, et al. EAACI allergen immunotherapy user's guide. *Pediatr Allergy Immunol* 2020;**31**(Suppl 25):1−101.
12. Kiel MA, Röder E, Gerth van Wijk R, Al MJ, Hop WC, Rutten-van Mölken MP. Real-life compliance and persistence among users of subcutaneous and sublingual allergen immunotherapy. *J Allergy Clin Immunol* 2013;**132**:353−60.e2.
13. Wang J, Zhou YM, Zhang HL, Hu LH, Liu JT, Wang L, et al. Pathogenesis of allergic diseases and implications for therapeutic interventions. *Signal Transduct Targeted Ther* 2023;**8**:138.
14. Forman HJ, Zhang H. Targeting oxidative stress in disease: promise and limitations of antioxidant therapy. *Nat Rev Drug Discov* 2021;**20**:689−709.
15. Bowler RP, Crapo JD. Oxidative stress in allergic respiratory diseases. *J Allergy Clin Immunol* 2002;**110**:349−56.
16. Nadeem A, Chhabra SK, Masood A, Raj HG. Increased oxidative stress and altered levels of antioxidants in asthma. *J Allergy Clin Immunol* 2003;**111**:72−8.
17. Karadogan B, Beyaz S, Gelincik A, Buyukozturk S, Arda N. Evaluation of oxidative stress biomarkers and antioxidant parameters in allergic asthma patients with different level of asthma control. *J Asthma* 2022;**59**:663−72.
18. Ozaras R, Tahan V, Turkmen S, Talay F, Besirli K, Aydin S, et al. Changes in malondialdehyde levels in bronchoalveolar fluid and serum by the treatment of asthma with inhaled steroid and beta2-agonist. *Respirology* 2000;**5**:289−92.
19. Abdulnaby NK, Sayed AO, Shalaby NM. Predictive value of serum uric acid in hospitalized adolescents and adults with acute asthma. *Therapeut Clin Risk Manag* 2016;**12**:1701−8.
20. Wedes SH, Khatri SB, Zhang R, Wu W, Comhair SAA, Wenzel S, et al. Noninvasive markers of airway inflammation in asthma. *Clin Transl Sci* 2009;**2**:112−7.
21. Han M, Lee D, Lee SH, Kim TH. Oxidative stress and antioxidant pathway in allergic rhinitis. *Antioxidants* 2021;**10**:1266.
22. Wang YH, Cui CC, Sun HJ. Anti-inflammatory effect of mangiferin on an experimental model of allergic rhinitis through the inhibition of NF-κB signaling pathways. *J Environ Pathol Toxicol Oncol* 2020;**39**:357−64.
23. Piao CH, Fan YJ, Nguyen TV, Song CH, Chai OH. Mangiferin alleviates ovalbumin-induced allergic rhinitis *via* Nrf2/HO-1/NF-κB signaling pathways. *Int J Mol Sci* 2020;**21**:3415.
24. Bui TT, Fan Y, Piao CH, Nguyen TV, Shin DU, Jung SY, et al. *Piper nigrum* extract improves OVA-induced nasal epithelial barrier dysfunction *via* activating Nrf2/HO-1 signaling. *Cell Immunol* 2020;**351**:104035.
25. Koksal ZG, Uysal P, Erdogan O, Cevik O. The association between allergic rhinitis and airway dysfunction and nasal endothelial damage and oxidative stress. *Rhinology* 2023;**61**:272−82.
26. Qu Z, Sun JC, Zhang WN, Jqy, Zhuang CL. Transcription factor NRF2 as a promising therapeutic target for Alzheimer's disease. *Free Radic Biol Med* 2020;**159**:87−102.
27. Hayes JD, Dinkova-Kostova AT. The Nrf2 regulatory network provides an interface between redox and intermediary metabolism. *Trends Biochem Sci* 2014;**39**:199−218.
28. Miura G. Playing KEAP1-away. *Nat Chem Biol* 2019;**15**:2.
29. Takaya K, Suzuki T, Motohashi H, Onodera K, Satomi S, Kensler TW, et al. Validation of the multiple sensor mechanism of the Keap1−Nrf2 system. *Free Radic Biol Med* 2012;**53**:817−27.
30. O'Connell MA, Hayes JD. The Keap1/Nrf2 pathway in health and disease: from the bench to the clinic. *Biochem Soc Trans* 2015;**43**:687−9.
31. Sun Y, Xu LJ, Zheng DP, Wang J, Liu GD, Mo ZX, et al. A potent phosphodiester Keap1−Nrf2 protein−protein interaction inhibitor as the efficient treatment of Alzheimer's disease. *Redox Biol* 2023;**64**:102793.
32. Villeneuve NF, Lau A, Zhang DD. Regulation of the Nrf2−Keap1 antioxidant response by the ubiquitin proteasome system: an insight into cullin-ring ubiquitin ligases. *Antioxidants Redox Signal* 2010;**13**:1699−712.

33. Dinkova-Kostova AT, Copple IM. Advances and challenges in therapeutic targeting of NRF2. *Trends Pharmacol Sci* 2023;**44**:137−49.
34. Lu MC, Ji JA, Lv YF, Zhao J, Liu YT, Jiao Q, et al. Bivalent inhibitors of the BTB E3 ligase KEAP1 enable instant NRF2 activation to suppress acute inflammatory response. *Cell Chem Biol* 2024;**31**: 1188−202.e10.
35. Liu GD, Hou RL, Xu L, Zhang XQ, Yan JY, Xing CG, et al. Crystallography-guided optimizations of the keap1−Nrf2 inhibitors on the solvent exposed region: from symmetric to asymmetric naphthalenesulfonamides. *J Med Chem* 2022;**65**:8289−302.
36. Sun Y, Huang JX, Chen YF, Shang H, Zhang WN, Yu JQ, et al. Direct inhibition of Keap1−Nrf2 protein−protein interaction as a potential therapeutic strategy for alzheimer's disease. *Bioorg Chem* 2020;**103**: 104172.
37. Wienken CJ, Baaske P, Rothbauer U, Braun D, Duhr S. Protein-binding assays in biological liquids using microscale thermophoresis. *Nat Commun* 2010;**1**:100.
38. Maniaci C, Hughes SJ, Testa A, Chen WZ, Lamont DJ, Rocha S, et al. Homo-PROTACs: bivalent small-molecule dimerizers of the VHL E3 ubiquitin ligase to induce self-degradation. *Nat Commun* 2017;**8**:830.
39. Haubrich K, Spiteri VA, Farnaby W, Sobott F, Ciulli A. Breaking free from the crystal lattice: structural biology in solution to study protein degraders. *Curr Opin Struct Biol* 2023;**79**:102534.
40. Wei JL, Meng FY, Park KS, Yim H, Velez J, Kumar P, et al. Harnessing the E3 ligase KEAP1 for targeted protein degradation. *J Am Chem Soc* 2021;**143**:15073−83.
41. Bae SH, Sung SH, Oh SY, Lim JM, Lee SK, Park YN, et al. Sestrins activate Nrf2 by promoting p62-dependent autophagic degradation of Keap1 and prevent oxidative liver damage. *Cell Metab* 2013;**17**:73−84.
42. Chen W, Chen SF, Yan CH, Zhang YG, Zhang RH, Chen M, et al. Allergen protease-activated stress granule assembly and gasdermin D fragmentation control interleukin-33 secretion. *Nat Immunol* 2022;**23**:1021−30.
43. Zappia CD, Soto A, Granja-Galeano G, Fenoy I, Fernandez N, Davio CA, et al. Azelastine potentiates antiasthmatic dexamethasone effect on a murine asthma model. *Pharmacol Res Perspect* 2019;**7**:e00531.
44. Yan JY, Li TF, Miao ZY, Wang P, Sheng CQ, Zhuang CL. Homobivalent, trivalent, and covalent PROTACs: emerging strategies for protein degradation. *J Med Chem* 2022;**65**:8798−827.
45. Li J, Cai ZY, Li XW, Zhuang C. Natural product-inspired targeted protein degraders: advances and perspectives. *J Med Chem* 2022;**65**:13533−60.
46. Tsai JM, Nowak RP, Ebert BL, Fischer ES. Targeted protein degradation: from mechanisms to clinic. *Nat Rev Mol Cell Biol* 2024;**25**: 740−57.
47. Lu MC, Liu T, Jiao Q, Ji JA, Tao MM, Liu YJ, et al. Discovery of a Keap1-dependent peptide PROTAC to knockdown Tau by ubiquitination−proteasome degradation pathway. *Eur J Med Chem* 2018;**146**:251−9.
48. Du G, Jiang J, Henning NJ, Safaee N, Koide E, Nowak RP, et al. Exploring the target scope of KEAP1 E3 ligase-based PROTACs. *Cell Chem Biol* 2022;**29**:1470−81.e31.
49. Chen H, Nguyen NH, Magtoto CM, Cobbold SA, Bidgood GM, Guzman LGM, et al. Design and characterization of a heterobifunctional degrader of KEAP1. *Redox Biol* 2023;**59**:102552.
50. Park SY, Gurung R, Hwang JH, Kang JH, Jung HJ, Zeb A, et al. Development of KEAP1-targeting PROTAC and its antioxidant properties: *in vitro* and *in vivo*. *Redox Biol* 2023;**64**:102783.
51. Wang FQ, Zhan Y, Li MM, Wang LD, Zheng A, Liu CB, et al. Cell-permeable PROTAC degraders against KEAP1 efficiently suppress hepatic stellate cell activation through the antioxidant and anti-inflammatory pathway. *ACS Pharmacol Transl Sci* 2023; **6**:76−87.
52. Qi MM, Zhong H, Cheng ZY, Chen SJ, Xiao H, Shang J, et al. Discovery of NAFLD-improving agents by promoting the degradation of Keap1. *J Med Chem* 2023;**66**:9184−200.
53. Kargbo RB. Redefining neurodegenerative treatment: synergy of KEAP1, PROTACs, and inflammatory modulators. *ACS Med Chem Lett* 2024;**15**:167−8.
54. Pei J, Xiao YF, Liu XG, Hu WY, Sobh A, Yuan Y, et al. Piperlongumine conjugates induce targeted protein degradation. *Cell Chem Biol* 2023;**30**:203−213.e17.
55. Powell CE, Du GY, Bushman JW, He ZX, Zhang TH, Fischer ES, et al. Selective degradation-inducing probes for studying cereblon (CRBN) biology. *RSC Med Chem* 2021;**12**:1381−90.
56. Diehl CJ, Salerno A, Ciulli A. Ternary complex-templated dynamic combinatorial chemistry for the selection and identification of homo-PROTACs. *Angew Chem Int Ed Engl* 2024;**63**:e202319456.
57. He SP, Ma JH, Fang YX, Liu Y, Wu SC, Dong GQ, et al. Homo-PROTAC mediated suicide of MDM2 to treat non-small cell lung cancer. *Acta Pharm Sin B* 2021;**11**:1617−28.
58. Yang WG, Liu WJ, Li X, Yan J, He WX. Turning chiral peptides into a racemic supraparticle to induce the self-degradation of MDM2. *J Adv Res* 2023;**45**:59−71.
59. Junk L, Schmiedel VM, Guha S, Fischel K, Greb P, Vill K, et al. Homo-bacPROTAC-induced degradation of ClpC1 as a strategy against drug-resistant mycobacteria. *Nat Commun* 2024;**15**:2005.
60. Yan JY, Li Y, Ding L, Hou RL, Xing CG, Jiang CS, et al. Fragment-based discovery of azocyclic alkyl naphthalenesulfonamides as Keap1−Nrf2 inhibitors for acute lung injury treatment. *J Med Chem* 2023;**66**:8267−80.
61. Zhang L, Xu LJ, Chen HH, Zhang WN, Xing CG, Qu Z, et al. Structure-based molecular hybridization design of Keap1−Nrf2 inhibitors as novel protective agents of acute lung injury. *Eur J Med Chem* 2021;**222**:113599.
62. Wheatley LM, Togias A. Clinical practice. Allergic rhinitis. *N Engl J Med* 2015;**372**:456−63.
63. Waage J, Standl M, Curtin JA, Jessen LE, Thorsen J, Tian C, et al. Genome-wide association and HLA fine-mapping studies identify risk loci and genetic pathways underlying allergic rhinitis. *Nat Genet* 2018; **50**:1072−80.
64. Yang ZX, Liang CQ, Wang TY, Zou QY, Zhou MX, Cheng Y, et al. NLRP3 inflammasome activation promotes the development of allergic rhinitis *via* epithelium pyroptosis. *Biochem Biophys Res Commun* 2020;**522**:61−7.
65. Wise SK, Damask C, Roland LT, Ebert C, Levy JM, Lin S, et al. International consensus statement on allergy and rhinology: allergic rhinitis-2023. *Int Forum Allergy Rhinol* 2023;**13**:293−859.